MAX-PLANCK-INSTITUT FÜR PLASMAPHYSIK

GARCHING BEI MÜNCHEN

DYNAMICS OF DECAYING TWO-DIMENSIONAL MAGNETOHYDRODYNAMIC TURBULENCE

Dieter Biskamp and Helmut Welter

IPP 6/279 December 1988

Abstract

High-resolution numerical studies of decaying two-dimensional magnetohydrodynamic turbulence using up to 768^2 modes in general periodic systems reveal the following properties: i) the evolution proceeds in a quasi-selfsimilar way with constant kinetic to magnetic energy ratio and constant micro- and macro-scale Reynolds numbers; ii) the energy dissipation rate is independent of the values of the dissipation coefficients η, μ; iii) the inertial-range energy spectra follow a Kolmogorov law, $E_k = C\epsilon^{2/3}k^{-5/3}$ with $C = 3.7 \pm 0.3$. Small-scale fluctuations are concentrated in the region of weak large-scale magnetic fields. The resulting strong intermittency is analogous to the behavior recently observed in two-dimensional hydrodynamic turbulence (see, for instance, J. Fluid Mech. (1988) 194, 333), with the magnetic field intensity taking the role vorticity plays in hydrodynamic systems.

Die nachstehende Arbeit wurde im Rahmen des Vertrages zwischen dem Max-Planck-Institut für Plasmaphysik und der Europäischen Atomgemeinschaft über die Zusammenarbeit auf dem Gebiete der Plasmaphysik durchgeführt.

I Introduction

Turbulence developing in high-Reynolds-number fluids is a fascinating physical phenomenon which has been attracting the interest of experimentalists as well as theoreticians for many decades, but which still defies satisfactory elucidation in spite of the considerable progress made. Most investigations deal with turbulence in simple incompressible fluids, described by the Navier-Stokes equations. Many methods and tools in turbulence theory have been invented for or adopted from other branches of theoretical physics to Navier-Stokes turbulence. One of these tools is direct numerical solution of the primitive fluid equations. Here the major problem is that of adequate spatial resolution, since the very nature of turbulence at high Reynolds numbers involves simultaneous excitation of different scales over a wide range. Therefore two-dimensional systems, which obviously allow higher spatial resolution, have drawn considerable attention in spite of their artificial nature. Recently, high-resolution numerical studies of two-dimensional Navier-Stokes turbulence[1)2)3)4)] yielded interesting new results. Depending on the initial or driving conditions, one finds either truly turbulent states with an inertial-range spectrum $E_k \propto k^{-3}$ or strongly intermittent states of weakly interacting coherent soliton-like structures with steeper energy spectra. In both cases, however, the two-dimensional case is basically different from the three-dimensional one with a Kolmogorov spectrum $E_k \propto k^{-5/3}$ and only weak intermittency effects. The origin of this difference is the simultaneous inviscid conservation of both energy and mean square vorticity in two dimensions, resulting in an inverse energy cascade and energy dissipation rates inversely proportional to the Reynolds number.

In electrically conducting fluids the dynamics is strongly influenced by magnetic fields, which in general will be present even in the absence of external fields owing to selfexcitation, i.e. dynamo action. The appropriate primitive equations are those of magnetohydrodynamics (MHD). It has been argued[5)6)] that 2D MHD turbulence should be more closely connected with the three-dimensional case than are two- and three-dimensional Navier-Stokes turbulence. In fact, in MHD both 2D and 3D exhibit a normal energy cascade to small scales and an inverse cascade of a quantity related to the magnetic potential, leading

to the buildup of large-scale quasi-static magnetic fields. In contrast to Navier-Stokes turbulence, for which various kinds of relatively simple laboratory or other kinds of terrestrial experiments can be performed, such experiments are difficult in the MHD case owing to the lack of suitable conducting fluids. A tank 1 m in diameter filled with mercury moving at an average velocity of 1 m/s has a magnetic Reynolds number of only about 10. (Only in liquid-metal-cooled breeder reactors are higher Reynolds numbers reached.) MHD turbulence in plasmas occurs in devices developed in controlled nuclear fusion research as well as in astrophysical systems, notably the solar wind, but while in the latter the conditions for turbulence generation are not controlled, in the former diagnostics is difficult. Numerical simulations are therefore particularly important to understand the dynamic properties of high-Reynolds-number conducting fluids.

In this paper we describe the results of a series of high-resolution computations of decaying 2D MHD turbulence. Choosing different kinds of initial states as well as varying the dissipation coefficients, we try to obtain a fairly general picture of the turbulent dynamics. The paper is organized as follows. In section II we briefly outline some basic properties of MHD turbulence. The numerical procedure and the choice of initial states are described in section III. If the initial ratio of kinetic to magnetic energy is of the order of unity or larger, it is found that the configuration decays in a statistically selfsimilar fashion, the macroscopic properties of which are described in section IV. Section V treats the generation of small-scale turbulent fluctuations, giving rise to Kolmogorov-type inertial-range spectra and energy dissipation rates independent of the value of the resistivity. For small initial values of the kinetic to magnetic energy ratio the system first exhibits a turbulent phase which then leads to a quasi-coherent phase characterized by pairwise coalescence of magnetic flux tubes, as described in section VI. Section VII gives the conclusions.

II Basic properties of MHD turbulence

Two-dimensional incompressible MHD has two independent dynamic variables, conveniently chosen as the magnetic flux function ψ, $\vec{B} = \hat{z} \times \nabla\psi$ and the velocity stream function ϕ , $\vec{v} = \hat{z} \times \nabla\phi$ (z being the ignorable coordinate), obeying the equations

$$\frac{\partial\psi}{\partial t} + \vec{v} \cdot \nabla\psi = \eta\nabla^2\psi \ , \tag{1}$$

$$\frac{\partial w}{\partial t} + \vec{v} \cdot \nabla w = \vec{B} \cdot \nabla j + \mu\nabla^2 w \ , \tag{2}$$

$$w = \nabla^2\phi \quad , \quad j = \nabla^2\psi \quad ,$$

η , μ being the dissipative coefficients, i.e. the magnetic diffusivity and the kinematic viscosity. The density ρ is assumed to be uniform. With the normalization $\rho = 1$, B assumes the dimension of a velocity. In contrast to 2D hydrodynamics, i.e. eq. (2) with $B = 0$, the vorticity is not merely convected but may also be enhanced by magnetic tension, $\vec{B} \cdot \nabla j$ in eq. (2). It follows from (1) , (2) that there are three global quantities quadratic in ψ and ϕ , which are conserved in the limit $\eta, \mu \to 0$,

$$E = \frac{1}{2}\int \left(v^2 + B^2\right) d^2x \quad , \tag{3}$$

$$H = \int \vec{v} \cdot \vec{B} d^2x \quad , \tag{4}$$

$$K = \int \psi^2 d^2x \quad , \tag{5}$$

the total energy, the cross helicity, and the mean square magnetic potential, respectively. Equilibrium statistical mode distributions suggest that in the presence of finite dissipation the spectral densities of the first two quantities E_k and H_k exhibit a normal cascade to large wave numbers, while K_k shows an inverse cascade leading to increasingly large-scale magnetic structures. Let us compare the relation of two- and three-dimensional geometry for Navier-Stokes and MHD turbulence.

The two-dimensional Navier-Stokes equation has two inviscid quadratic invariants, the energy $E = \frac{1}{2}\int v^2 d^2x$ and the mean square vorticity or enstrophy $W = \int \left(\nabla \times \vec{v}\right)^2 d^2x = \int w^2 d^2x$, with W_k exhibiting a normal cascade and E_k an inverse cascade, i.e. mode energy

propagates to longer wavelengths away from the dissipative scales. In fact, in a decaying 2D turbulence field the energy dissipation rate $\epsilon \equiv -dE/dt = \mu W$ decreases in time $\epsilon(t) < \epsilon(0) = O(\mu)$, a consequence of inviscid enstrophy conservation and monotonic viscous decay $dW/dt = -\mu \int (\nabla w)^2 \, d^2x$. In three-dimensional Navier-Stokes turbulence only the energy is inviscidly conserved with the spectral energy density cascading to large k , and the energy dissipation rate is independent of μ , as the vorticity may assume arbitrarily large values. By contrast the formal difference between two- and three-dimensional MHD is significantly smaller. As in 2D, the three-dimensional system has three inviscid invariants, viz. energy and cross helicity as in 2D and the magnetic helicity $\int \vec{A} \cdot \vec{B} d^3x$ instead of the mean square magnetic potential. It has been argued[6] that 2D MHD flows behave like hydrodynamic turbulence in a dimension intermediate between two and three. In this paper we shall see that 2D MHD flows develop turbulent structures in regions of finite extent with characteristic features usually attributed only to fully three-dimensional turbulent flows.

A feature that distinguishes MHD flows from nonmagnetic hydromagnetic flows is the presence of a large-scale magnetic field. In contrast to a large-scale flow which can be locally eliminated by a Galilean transformation, the magnetic field has a profound effect on the turbulent dynamics. Two extreme cases may be distinguished : a) The magnetic field is weak in relation to the turbulent velocities. This situation is primarily connected with the dynamo problem of magnetic field amplification and, because of the anti-dynamo theorem[7], usually requires a three-dimensional velocity field and hence a fully three-dimensional treatment. b) The mean field is large compared with turbulent flow velocities. In this case the flow is highly anisotropic. While the perpendicular motions may develop small dissipative scales, i.e. give rise to turbulent dissipation, spatial variations along the mean field generally remain smooth, their dynamics being determined by the weak interaction of Alfvén waves. It is therefore argued that local two-dimensional dynamics perpendicular to a strong mean field describe an essential part of the fully three-dimensional problem, whereas two-dimensional modelling including a mean field within the plane considered, though interesting in itself, is less representative of a three-dimensional system because it

ignores the major turbulent dissipation process. We therefore assume in the present two-dimensional studies that there is no mean field component in the computational plane, thus modelling systems with a strong perpendicular mean field.

In two-dimensional systems dissipation takes place primarily in the regions of weak magnetic field, i.e. neutral points, where large current densities may be generated. Since, however, localized dissipation of magnetic energy necessarily implies mass transport from outside regions, where the frozen-in condition is satisfied, into the dissipative region, only X-type neutral points allow rapid dissipation, the inflowing mass being ejected sideways along the magnetic field. In O-type neutral points mass accumulation prevents enhanced dissipation, which can only proceed on the overall slow resistive time scale.

A characteristic feature of a turbulent fluid is its inertial-range energy spectrum, where the inertial range is loosely defined as the region of k-space located between the small energy-carrying wave numbers, where excitation and geometry effects are important, and the large wave numbers, where dissipation dominates. (For the inertia range to be clearly discernible the Reynolds number has to be sufficiently high.) If a local transfer process in k-space (corresponding to the picture of a cascade with sufficiently small steps) is assumed, energy spectra follow from simple scaling considerations[8]. In the case of a normal energy cascade this predicts the $E_k \propto k^{-5/3}$ spectrum, while for a normal enstrophy cascade one obtains $E_k \propto k^{-3}$. Here E_k is defined in such a way that $\int E_k dk$ is the total turbulent energy per volume. Note that the result is independent of the spatial dimension and the manner of turbulence excitation and dissipation. It, however, assumes statistical homogeneity and isotropy. In the case of MHD turbulence a modification of Kolmogorov's argument has been suggested[9][10], leading to a slightly flatter inertial-range spectrum $E_k \propto k^{-3/2}$. The basic mechanism is that in the presence of large-scale magnetic structures B_l (not necessarily a static mean field) small-scale fluctuations behave essentially as Alfvén waves which has the consequence that $v_k^2 = B_k^2$ for modes in the inertial range. The argument can be made more quantitative by introducing the Elsässer variables $\vec{E}_\pm = \vec{v} \pm \vec{B}$ instead of $\vec{v}$, $\vec{B}$ in the MHD equations. Since only mixed nonlinear terms $E_+ E_-$ appear, corresponding to Alfvén waves propagating in opposite directions – the absence of terms

E_+E_+ or E_-E_- implies that Alfvén waves do not steepen – , the interaction time of two wave packets of mean wave number k is short, $\tau \sim (B_l k)^{-1}$. The energy transfer rate in the inertial range, which for stationary turbulence equals the energy dissipation rate ϵ , is proportional to the mode interaction time, the proportionality factor being a function of the energy spectrum E_k and k only, on the assumption of a local cascade. From dimensional analysis one obtains

$$\epsilon = A \frac{1}{B_l k} E_k^2 k^4 \tag{6}$$

and hence

$$E_k^2 \propto k^{-3/2} \quad . \tag{7}$$

(In hydrodynamic turbulence the interaction time is much longer $\tau \propto (v_k k)^{-1} = (E_k k^3)^{-1/2}$, which inserted into eq. (6) instead of $(B_l k)^{-1}$ gives the Kolmogorov spectrum.) We shall see, however, that this Alfvén wave argument does not seem to hold, at least not in the case of 2D MHD turbulence.

There has been considerable discussion about self-organization in MHD, either by selective decay[11)12)] or by dynamic alignment[13)14)] . Selective decay is primarily connected with the different decay rates of the inviscid invariants,

$$\frac{dE}{dt} = -\eta \int j^2 d^2x - \mu \int w^2 d^2x \quad , \tag{8}$$

$$\frac{dH}{dt} = -(\eta + \mu) \int jw d^2x \quad , \tag{9}$$

$$\frac{dK}{dt} = -\eta \int (\nabla \psi)^2 d^2x \quad . \tag{10}$$

Evidently, since the r.h.s. of eqs. (8), (9) contain derivatives of higher order than that of eq. (10), E and H decay more rapidly than K. (Another manifestation of this effect is that E_k, H_k show a normal cascade, while K_k follows an inverse cascade.) However, while the r.h.s. of (8) is negative definite, the r.h.s. of (9) may have either sign, and hence H may effectively decay more slowly than E. This could lead to a more and more aligned state, $\vec{v} \parallel \vec{B}$. Such aligned states have been observed as a predominant feature in the solar wind[14)] . The interpretation of these observations, however, is still under discussion since

the solar wind is an open system and the alignment may just be due to spatial separation of $\vec{E}_+$ and $\vec{E}_-$ waves and not to a generic property of a closed decaying turbulent system. In the present studies we are more interested in the turbulent decay process itself, and certain selfsimilar properties that arise during the decay, than in the final states. For the cases considered, which avoid strongly aligned initial configurations, dynamic alignment is not found to be a conspicuous effect, and the discussion given by Ting et al.[12] does not apply.

III Numerical procedures and initial states

Equations (1) and (2) are solved in a rectangular box of size $L_x = L_y = 2\pi$ with periodic boundary conditions. We use a fully dealiased pseudo-spectral method with M^2 modes, where dealiasing is achieved in the simple and efficient way by setting mode amplitudes f_{k_x,k_y} with $|k_x|$ or $|k_y| \geq M/3$ equal to zero. This means that only $(2/3)^2 M^2$ modes are actually computed and stored. Complete M^2 arrays are only needed to compute the convolutions using fast Fourier transforms. As a result systems with M up to 768 can be computed on a CRAY-XMP 2/4 with incore storage. Since the pseudo-spectral method has previously been discussed in many papers and books (see, for instance, Ref. 15), we do not describe it in any more detail.

We use somewhat more general dissipative terms than given in eqs. (1) and (2) :

$$\eta \nabla^2 \psi \longrightarrow \eta_{\nu-1} (-1)^{\nu-1} \nabla^{2\nu} \psi \ , \tag{11}$$

$$\mu \nabla^2 w \longrightarrow \mu_{\nu-1} (-1)^{\nu-1} \nabla^{2\nu} w \ , \tag{12}$$

where $\nu = 1$ corresponds to normal diffusion and $\nu = 2$ is sometimes called hyperdiffusion. $\nu > 1$ is often used in numerical studies to obtain a clearer separation of the dissipative scales from the inertial range (ν-values as high as 8 are found in the literature, e.g. Ref. 4). In the present studies we restrict ourselves to $\nu = 1$ and 2 .

The numerical accuracy can in principle be controlled by the deviations from the integral conservation relations eqs. (8) - (10) . However, since E, H, K are so-called rugged invariants[16], i.e. are (inviscidly) conserved not only in integral form but also in a truncated finite Fourier approximation, only the time discretization error $(\propto \Delta t^2)$ can be detected. Spatial resolution is checked more empirically. It turns out that good resolution requires the energy spectrum to decay monotonically at the high k edge. (By the way, numerical instability occurring for Δt exceeding the stability threshold first shows up in the k-spectrum.) Also inspection of the j or w contour plots gives rather reliable information on the quality of the spatial resolution. There has been some discussion about the necessity and usefulness of dealiasing in pseudo-spectral computations; see, for instance,

Ref. 15. Though the aliasing errors are formally of the same order as the error introduced by truncation of the Fourier series, we find in our computations that the global error is actually a factor of $10 - 100$ larger in the non-dealiased system. The error appears most distinctly at the high-k modes, strongly enhancing the tendency of the system to become numerically unstable. Only for $\nu \geq 2$ have long-time non-dealiased computations been possible.

Since we are considering decaying turbulence, the choice of the initial state is of primary importance. To be typical in the sense of having finite probability in real flows, the initial state should not be too symmetric or have other unusual properties such as high velocity-magnetic field correlations. We therefore refrained from applying high symmetry conditions to obtain a formally large ratio k_{max}/k_{min}, as has recently been done for 2- and 3-dimensional hydrodynamic simulations[1)17)], because these might also influence the small-scale dynamics. We consider essentially two different types of initial states. Systems A_1 and A_2 represent large-scale configurations.

$$\begin{aligned} \phi_{A_1}(x,y) &= cos(\ x + 1.4) + cos(y + 0.5) \quad , \\ \psi_{A_1}(x,y) &= cos(2x + 2.3) + cos(y + 4.1) \quad ; \end{aligned} \tag{13}$$

$$\begin{aligned} \phi_{A_2} &= \phi_{A_1} \quad , \\ \psi_{A_2} &= \frac{1}{3}\psi_{A_1} \quad . \end{aligned} \tag{14}$$

The phases are just arbitrary numbers with no particular significance. The configuration A_1 is characterized by a ratio of kinetic to magnetic energy $E^V/E^M = 0.4$ and a velocity-magnetic field correlation $H/E = 0.28$. It constitutes a generalization of the Orszag–Tang vortex[6)]

$$\begin{aligned} \phi_{OT}(x,y) &= cos\, x + cos\, y \quad , \\ \psi_{OT}(x,y) &= \frac{1}{2}cos\, 2x + cos\, y \quad , \end{aligned} \tag{15}$$

with $E^V/E^M = 1$ and $H/E = 0.5$, which is used in the recent literature as a reference system and which we, too, shall briefly consider for comparison. System A_2 differs from A_1 only in the magnitude of the magnetic potential, having $E^V/E^M = 3.6$ and $H/E = 0.256$.

System B contains a broad spectrum of modes

$$\phi_{B\vec{k}} = a\, exp\left\{-k^2/2k_0^2 + i\alpha_{\vec{k}}\right\} \quad ,$$
$$\psi_{B\vec{k}} = a\, exp\left\{-k^2/2k_0^2 + i\beta_{\vec{k}}\right\} \quad , \tag{16}$$

where $k^2 = k_x^2 + k_y^2$, $k_x, k_y = \pm 1, \pm 2, \ldots$, and the normalizing factor a is chosen such that $E = 1$. Obviously, one has $E^V/E^M = 1$ in this case; we choose $k_0 = 5$, and $\alpha_{\vec{k}}, \beta_{\vec{k}}$ are random phases. The value of the velocity-magnetic field correlation H/E depends on the particular phase realization. We only consider $\eta = \mu$, i.e. unit magnetic Prandtl number. Different values of the resistivity are chosen, $\eta_0 = 2.5 \times 10^{-3}, 1.25 \times 10^{-3}, 6.25 \times 10^{-4}, 3.125 \times 10^{-4}$ for $\nu = 1$ and $\eta_1 = 6.8 \times 10^{-8}, 10^{-8}$ for $\nu = 2$. In all cases spatial resolution characterized by the number of modes M is adequate, with $k_d \lesssim k_{max} = M/3$ where $k_d = \left(\epsilon/\eta_0^3\right)^{1/4}$ for $\nu = 1$ and $\left(\epsilon/\eta_1^3\right)^{1/10}$ for $\nu = 2$, ϵ is the energy dissipation rate.

The relative size of the dissipative effects is characterized by various types of Reynolds numbers. We distinguish between magnetic and kinetic (using superscripts V and M) as well as macro- and micro-scale Reynolds numbers (subscripts Λ and λ) ,

$$R_\Lambda^V = \frac{\sum\limits_k k|\phi_k|^2}{\mu\left(\sum\limits_k k^2|\phi_k|^2\right)^{\frac{1}{2}}} \quad , \tag{17}$$

$$R_\lambda^V = \frac{\sum\limits_k k^2|\phi_k|^2}{\mu\left(\sum\limits_k k^4|\phi_k|^2\right)^{\frac{1}{2}}} \quad , \tag{18}$$

and analogous expressions for the magnetic Reynolds numbers $R_{\Lambda,\lambda}^M$ obtained by replacing ϕ by ψ and μ by η. The physical meaning of macro-scale Λ and micro-scale λ are the width of the velocity or magnetic field correlation functions and the curvature radii of these correlation functions at the origin, respectively. (One can prove that $\lambda < \Lambda$ under quite general conditions.) These Reynolds numbers are inherent dynamic quantities; we avoid the simple definition $R \propto L$, where L is the computational box size.

Various types of one-dimensional spectra may be introduced, corresponding to either longitudinal or lateral velocity correlation functions :

$$E_{\|k_x}^V = \sum_{k_y} |v_{xk}|^2 = \sum_{k_y} k_y^2 |\phi_k|^2 \quad , \tag{19}$$

$$E^V_{\|k_y} = \sum_{k_x} |v_{yk}|^2 = \sum_{k_x} k_x^2 |\phi_k|^2 \quad , \tag{20}$$

$$E^V_{\perp k_x} = \sum_{k_y} |v_{yk}|^2 = \sum_{k_y} k_x^2 |\phi_k|^2 \quad , \tag{21}$$

$$E^V_{\perp k_y} = \sum_{k_x} |v_{xk}|^2 = \sum_{k_x} k_y^2 |\phi_k|^2 \quad , \tag{22}$$

and analogous expressions for the magnetic field correlation functions $E^M_{\|k_x}$ etc. are obtained by replacing ϕ_k by ψ_k . For isotropic turbulence (19), (21) are identical to (20), (22), respectively. If the main part of the energy resides in the largest possible modes, as in cases corresponding to $A_{1,2}$ initial conditions, overall isotropy cannot be expected, but only local isotropy, i.e. spectra (19) and (20) should be identical only in the inertial and dissipative spectral ranges, not for the energy-containing mode numbers. In the case of (local) isotropy we conveniently consider the radial spectra

$$E^V_k = \frac{1}{2} \sum_{k'-\frac{1}{2} \le k < k'+\frac{1}{2}} k'^2 |\phi_{k'}|^2 \quad , \tag{23}$$

$$E^M_k = \frac{1}{2} \sum_{k'-\frac{1}{2} \le k < k'+\frac{1}{2}} k'^2 |\psi_{k'}|^2 \quad . \tag{24}$$

At this point we want to emphasize that the spectra taken at a particular instant in time or averaged over a certain time interval do not give information (or only very indirectly) on how turbulent the system is, in the usual intuitive sense. An MHD system containing only isolated current sheets, which would usually not be called turbulent, gives rise to a k^{-2} energy spectrum, which is only somewhat steeper than the Kolmogorov spectrum. On the same lines, mode number spectra give no indication of spatial intermittency, which seems to be a typical feature of 2D turbulence; see Ref. 1 for the hydrodynamic case and sections V and VI of this paper for the MHD case. So the emphasis here will be more on direct investigation of spatial structures.

IV Selfsimilar turbulent evolution

Starting from type A_2 (eq. 14) or B (eq. 16) initial states, for which $E^V/E^M \geq 1$, the system is found to relax quickly to a turbulent state, with the subsequent evolution proceeding in a statistically selfsimilar way. This evolution is characterized by constant Reynolds numbers R_Λ, R_λ and a constant ratio E^V/E^M, while the total energy E decays to a small fraction of its initial value. Figure 1 refers to system A_2 with $\eta = 6.25\times10^{-4}$ and $M = 512$. The eddy turnover time computed for the initial state is $\tau_0 = \left(\sum_k k^4|\phi_k|^2\right)^{-\frac{1}{2}} = 1$ ($\simeq 1/\langle k\rangle\langle v\rangle$). Figure 1a gives the total energy E and the energy ratio E^V/E^M. During the initial relaxation phase for $t \lesssim 3$ the energy is roughly constant because turbulent dissipative small scales are gradually excited (details of this process are discussed in section V). Subsequently, the energy decays while the ratio E^V/E^M remains about constant, $E^V/E^M \simeq 0.5$. It is also quite independent of the value of η_0. In Fig. 1b,c the time evolution of the Reynolds numbers $R_\Lambda^{V,M}$, $R_\lambda^{V,M}$ is plotted. Obviously, the initial values have little relation to the quasi-constant values in the turbulent state. It is interesting to see how these quantities depend on the resistivity. Figure 2 shows R_Λ^M, R_λ^M for three values $\eta_0 = 3.125\times10^{-4}$, 6.25×10^{-4}, 1.25×10^{-3} in the selfsimilar phase $t \gtrsim 5$. While the macro-scale Reynolds number is proportional to η_0^{-1}, the micro-scale Reynolds number increases less strongly $R_\lambda^M \propto \eta^{-\alpha}$, with $\alpha \simeq 2/3$. The latter behavior can be understood qualitatively from the definition of R_λ^M, eq. (20). With $\eta\sum_k k^4|\psi_k|^2 \sim \epsilon$, we find $R_\lambda^M \sim \left(\eta\epsilon/E^2\right)^{-\frac{1}{2}} \sim \eta^{-\frac{2}{3}}$ since ϵ/E^2 is found to be roughly $\sim \eta^{1/3}$ (and constant in time; see discussion in section V). Figure 3 refers to system B, for $\eta_0 = 1.25\times10^{-3}$, $M = 512$, and $H/E = 0.258$ for this choice of random phases $\alpha_{\vec{k}}$, $\beta_{\vec{k}}$, giving diagnostics as in Fig. 1. The eddy turnover time is smaller than for A_2, $\tau_0 = 0.1$, mainly owing to the smaller dominant scales, with the maximum of E_k at $k \sim 10$. Hence the initial relaxation time is much shorter and the total time $t = 6$ is effectively longer than $t = 16$ for system A_2, with the energy decaying to a smaller fraction. Figure 4 gives the temporal behavior of the Reynolds number for $\eta_0 = 6.25\times10^{-4}$, 1.25×10^{-3}, 2.5×10^{-3} analogously to Fig. 2. The constancy of E^V/E^M and the Reynolds numbers is remarkable since the configuration strongly changes during this time, with spatial scales increasing by a factor of 3 and field

amplitudes decreasing by roughly the same factor.

In a recent article[18] somewhat related properties of 2D MHD turbulence were investigated, where the presence and persistence of oscillations in the ratio E^V/E^M was particularly emphasized. It seems to us, however, that starting with an arbitrary dynamic MHD state, magnetic oscillations are a natural consequence. The amplitude of the oscillations in the ratio E^V/E^M depends on the degree of coherence of the large-scale velocities and fields. While for system A_2 dominated by $k \sim 1$ modes the amplitude is rather significant, $\sim 20\%$ (see Fig. 1a), it is smaller for system B with dominant modes at $k \gg 1$ (Fig. 3a). The persistence of the E^V/E^M oscillation is not surprising either. Since the damping is caused by the same turbulent dissipation process as the decay of the total energy, the two decay rates should be similar in that the relative amplitudes are constant. It is, however, rather unexpected that the behavior in the relaxed selfsimilar phase is independent of the initial value of E^V/E^M, at least for $E^V/E^M \gtrsim 1$. (For $E^V(0)/E^M(0) < 0.5$ the behavior is somewhat different, as will be discussed in section VI.) The quasi-stationary value of E^V/E^M depends somewhat on the initial velocity-magnetic field correlation H/E. Figure 5 gives this ratio for two B-type realizations, the upper curve for $H/E = 0.258$ as in Fig. 3a, the lower one for $H/E = 0.023$, i.e. almost vanishing correlation. The difference in the average values is rather small, smaller than suggested by Fig. 4 in Ref. 18. We do not consider more highly correlated states with $H/E \gtrsim 0.5$.

Concerning the phenomenon of selective decay, it is interesting to compare the evolution of E, H, K for different values of η. Figure 6 gives these quantities for type-A_2 initial state and the three values of η used in Fig. 2. There is a clear tendency with small η for E and H to decay at about the same finite rate, while K decays on a much longer time scale.

V Small scale turbulence and dissipation

In 2D hydrodynamic turbulence energy dissipation is small, $\epsilon = O(\mu)$, $\epsilon(t) < \epsilon(0)$, which is a consequence of inviscid enstrophy conservation and the inverse cascade of the energy in mode number space. Only enstrophy may be dissipated at a finite rate. By contrast in 2D MHD flows energy dissipation rates were found to increase strongly, $\epsilon(t) \gg \epsilon(0)$[6], though ϵ still appears to depend on η. It is therefore interesting to study this point by means of the present computations, which have higher resolution and thus allow higher Reynolds numbers than those of Ref. 6. When comparing systems with identical initial states but different values of η, μ, we should consider the relative dissipation rate $\hat{\epsilon}(t) = -(dE/dt)/E$ instead of $\epsilon(t)$, since during the first relaxation period where turbulence is generated, dissipation in the lower η system is invariably smaller, leaving the system at a somewhat higher value of E at the beginning of the turbulent phase than in a system with larger η. (To be specific ϵ always refers to the change of the energy per unit volume, $E = \sum_k E_k$.) Though the effect is rather small, normalization to the instantaneous value of E makes the comparison of cases with different η more convincing. Figure 7 gives $\hat{\epsilon}(t)$ for three cases with A_2 initial conditions and $\eta_0 = 1.25 \times 10^{-3}$, 6.25×10^{-4}, 3.125×10^{-4}, the same cases shown in Figs. 2 and 6. For $t \lesssim 2$ the dynamics is independent of η and hence $\hat{\epsilon} \simeq \epsilon \propto \eta$. The maxima of $\hat{\epsilon}$, reached at slightly later times for smaller η, still differ systematically, $\hat{\epsilon} \propto \eta^{1/4}$, but in the subsequent turbulent phase $\hat{\epsilon}$ soon becomes essentially independent of η apart from random variations due to the differences in small-scale dynamics. Similar behavior is found for type-B initial conditions, plotted in Fig. 8 for $H/E = 0.258$ and $\eta_0 = 2.5 \times 10^{-3}$, 1.25×10^{-3}, 6.25×10^{-4}, the same cases as shown in Fig. 4.

It is also interesting to consider the temporal behavior of the energy decay. B-type systems are particularly interesting since conditions significantly vary (for instance, the macro-scale changes by a factor of more than 3) without restrictions due to finite box size becoming important. As seen in Fig. 9, referring to the same cases as in Fig. 4, the quantity ϵ/E^2 is approximately constant in time,

$$-\frac{1}{E^2}\frac{dE}{dt} \simeq \alpha \quad , \tag{25}$$

and hence

$$E(t) = \frac{1}{\alpha\,(t + t_0)} \quad . \tag{26}$$

We also see that in contrast to $\hat{\epsilon} = \epsilon/E$ (Fig. 8), ϵ/E^2 depends on η.

Let us now investigate the onset of turbulence in greater detail, using type-A_1 initial conditions, which are found to illustrate the different micro-scale processes particularly well. We consider contour plots of the current density j since j (and the vorticity w) emphasize small scales over large scales. Figure 10 shows the transition to turbulence for a case with high resolution $M = 768$ and large effective Reynolds number, viz. $\nu = 2$ and $\eta_1 = 10^{-8}$. At $t = 1.6$ thin current sheets are generated (Fig. 10a). Closer inspection reveals the basic features of quasi-stationary (Sweet-Parker) current sheets including fine structures at the sheet ends, which have previously been discussed in detail[19]. Figure 10b shows how this state of isolated, finite-length current sheets is modified at $t = 2.1$. Two different processes are clearly discernible : a) stretching and folding of the sheets, leading to elongation of the sheet, which is similar to the process of vorticity gradient sheet folding observed in 2D hydrodynamic turbulence[1]; b) tearing instability of the current sheets. Both processes lead to a dense distribution of small-scale sheets covering regions of finite extent, located in regions of weak magnetic field, mainly around X-points as seen in Fig. 11, where j- and ψ-contours are plotted at $t = 3$ for the same case as in Fig. 10. While process a) is intensified in a gradual fashion with decreasing η, the tearing mode exhibits a threshold behavior, as can be seen in Fig. 12, showing two states differing from Fig. 10b only in a somewhat stronger dissipation, both with $\nu = 1$, and $\eta_0 = 3.125 \times 10^{-4}$ in Fig. 12a, $\eta_0 = 6.25 \times 10^{-4}$ in Fig. 12b. Continuation of the latter case shows that the tearing instability does not appear at any time. As previously discussed[19], Sweet-Parker sheets are significantly more stable with respect to tearing modes than static current sheets, primarily owing to the inhomogeneous flow along the sheet, with a threshold $A \sim 100$ as compared with $A \sim 10$ in the static case, A being the ratio of sheet length to width. Since the sheets become thinner with decreasing η, instability will set in at sufficiently low η. On the other hand, the appearance of the tearing mode does not lead to a sudden increase of the dissipation rate, but its effect is becoming gradually stronger

with decreasing η. Figure 11 gives the dissipation rates for five cases, the upper four (cases 1-4) with $\nu = 1$, $\eta_0 = 2.5 \times 10^{-3}$, 1.25×10^{-3}, 6.25×10^{-4}, 3.125×10^{-4} and the lowest one (case 5) with $\nu = 2$ and $\eta_1 = 10^{-8}$. With decreasing dissipation coefficients, two-stage saturation behavior becomes more and more pronounced. At $t \simeq 1.5$ current sheets are formed. Comparing the values of ϵ at this time for the four different $\nu = 1$ cases, we find – not unexpectedly – that $\epsilon \propto \eta^{\frac{1}{2}}$. The further increase of ϵ is due to excitation of small scales by the processes described above until ϵ becomes independent of η. Comparison of cases 3 (tearing stable) and 4 (tearing unstable) shows that the tearing mode does not abruptly increase dissipation. This two-stage process is analogous to the behavior observed in two-dimensional hydrodynamic turbulence[1]. There first isolated vorticity gradient sheets are generated, which are subsequently folded in a turbulent way. Turbulence is intermittent with coherent structures surviving where vorticity is strong, and turbulent vorticity gradient sheets being concentrated in regions of small vorticity. In the MHD case the magnetic field takes the role vorticity plays in 2D hydrodynamics. (Owing to the possibility of the tearing mode the generation of turbulent fluctuations is, however, more effective in MHD.) Intermittency is the more pronounced the larger the magnetic energy, i.e. the smaller the initial value of E^V/E^M. Figure 14 illustrates a case with A_2 initial conditions with $E^V/E^M = 3.6$, which should be compared with Fig. 11, a case with A_1 initial conditions, i.e. $E_V/E_M = 0.4$. While in the latter case large nonpolluted coherent magnetic flux tubes exist, with small scale turbulence well confined to relatively small regions around the X-points, in the former case turbulent regions are broader and less clearly distinguishable from coherent magnetic structures.

We also studied the evolution of the Orszag-Tang vortex (eq. (15)) which has been considered in several previous articles (see, for instance, Refs. 18, 20). Compared with our $A_{1,2}$ cases, the tendency to generate turbulent small-scale structures is significantly weaker. Even for $\eta = 3.125 \times 10^{-4}$ (which corresponds to eight times the initial value of the Reynolds number considered by Orszag and Tang[6]) the state at $t = 3$ still consists mainly of isolated current sheets. This behavior could be a consequence of the higher velocity-magnetic field correlation $H/E = 0.5$ as compared with the value $H/E \lesssim 0.25$

considered in this paper. This point deserves further investigation. It should also be noted that the dynamic states following from the OT vortex have an additional symmetry apart from periodicity : $\psi(2\pi - x, 2\pi - y) = \psi(x, y)$, $\phi(2\pi - x, 2\pi - y) = \phi(x, y)$. Hence only half of the Fourier modes are actually independent. Even if one believes that restriction of the degrees of freedom by symmetry properties does not affect the transfer processes from large to small scales, which is debatable, the system is effectively only half the size, thus giving poorer statistics.

The behavior of the energy spectra reflects the dynamic picture described above, in particular the transition from isolated current sheets to densely packed, turbulent small-scale structures. Isolated coherent current sheets and the associated vortex sheets give rise to energy spectra $E_k^M, E_k^V \propto k^{-2}$. The most interesting spectral properties arise in the turbulent regime. We consider different spectra for the state given in Fig. 11. Comparison of $E^M_{\|k_x}$ and $E^M_{\|k_y}$, defined in eqs. (19), (20), an example being given in Fig. 15, indicates that apart from the smallest mode numbers the spectra are largely isotropic. Figure 16 gives the radial spectra $E_k^{M,V}$. An inertial range can be clearly seen, with a $-5/3$ rather than a $-3/2$ spectral exponent. Since the fluctuations with wave numbers in the inertial range $5 \lesssim k \lesssim 50$ are located primarily in regions of weak magnetic field, as can be clearly seen in Figs. 11, 14, Kraichnan's argument[10] for a $k^{-3/2}$ law in fact does not hold. Though $E_k^V \simeq E_k^M$, E_k^V is consistently slightly smaller than E_k^M. Hence the result $E^V/E^M < 1$ observed for the energy-containing modes seems to be valid for the entire spectrum.

It is interesting to investigate a possible similarity law of the evolution of the energy spectrum. Considering the normalized spectrum ${}^{\nu}\hat{E}\,(k/k_d)$

$$ {}^{1}\hat{E}\left(\frac{k}{k_d}\right) \equiv \frac{E_k}{(\epsilon\eta_0^5)^{1/4}} \quad , \quad k_d = \left(\frac{\epsilon}{\eta^3}\right)^{1/4} \text{for} \quad \nu = 1 \quad , $$

$$ {}^{2}\hat{E}\left(\frac{k}{k_d}\right) \equiv \frac{E_k}{(\epsilon\eta_1)^{1/2}} \quad , \quad k_d = \left(\frac{\epsilon}{\eta^3}\right)^{1/10} \text{for} \quad \nu = 2 \quad , $$

where $E_k = E_k^V + E_k^M$. Figure 17 gives the ${}^{1}\hat{E}(k/k_d)$-spectrum of a B-type case with $\eta_0 = 6.25 \times 10^{-4}$ taken at $t = 3, 4, 5, 6$. Obviously there exists a universal spectrum. In Fig. 18 the normalized energy spectrum ${}^{2}\hat{E}(k/k_d)$ of the A_1-type case with $\nu = 2$, $\eta_1 = 10^{-8}$,

illustrated in Figs. 10, 11, taken at $t = 2.5, 2.6, 2.7, 2.8$. Naturally the dissipative bend-over for $\nu = 2$ occurs much more localized at $k/k_d \simeq 0.5$ than for $\nu = 1$, Fig. 17, with the $k^{-5/3}$ inertial range behavior more clearly visible. For both $\nu = 1$ and $\nu = 2$ the Kolmogorov constant C characterizing the level of the inertial range spectrum, $E_k = C\epsilon^{2/3}k^{-5/3}$, is the same within the given accuracy, $C = 3.6 \pm 0.3$, as expected, since the type of dissipation should not affect the behavior in the inertial range. This value of C has to be contrasted with $C \simeq 1.7$ for 3D hydrodynamic turbulence. It is somewhat surprising that in our 2D MHD case the value of C is quite universal, independent on the different degree of intermittency in the A_1, A_2, and B type cases.

VI Coherent magnetic dynamics : coalescence

When ψ and ϕ contour plots evolving in time, are compared, only ψ exhibits clear, coherent structures, mainly magnetic monopoles, called flux tubes, which are convected according to eq. (1) without significant distortion (see Fig. 19). Their mutual interaction is different from that of vorticity macro-eddies in 2D hydrodynamics, discussed in Refs. 2-4. While the latter, if sufficiently sparse in space (at positions $\vec{x}_i$), move along equipotentials $\phi = const$,

$$\nabla^2\phi = \sum_i \alpha_i \delta(\vec{x} - \vec{x}_i) \quad ,$$

$$\vec{v} = \hat{z} \times \nabla\phi \quad ,$$

thus avoiding collisions, there is a radial magnetic force $\propto \nabla\psi$ between flux tubes as obtained by integrating eq. (2)

$$\frac{d\vec{v}}{dt} \cong -j\nabla\psi \quad ,$$

leading to an attraction of flux tubes with currents of equal sign. If the average velocity is sufficiently large, a flux tube exerts a quasi-random motion, interacting only weakly with its neighbors. Occasionally, magnetic attraction is strong enough to lead to complete coalescence of two flux tubes. Since resistive effects are stronger for smaller scales, small flux tubes coalesce more readily, which is the physical mechanism of the inverse ψ-cascade.

The tendency to coalesce is increased if the initial state has low kinetic energy, $E^V(0)/E^M(0) < 0.5$. In such a system E^V/E^M further decays in time in contrast to the selfsimilarly evolving systems with $E^V(t)/E^M(t) \sim 0.5$ discussed in section IV. Turbulent states with Reynolds-number-independent energy dissipation rates exist only for a transient period, leading to a phase dominated by magnetic forces, with pairwise coalescence being the main dynamic process and dissipation occurring mainly in quasi-stationary current sheets in between. Figure 20 gives $\hat{\epsilon}(t)$ for three cases with A_1 initial states, $\nu = 1$ type diffusion and $\eta_0 = 2.5 \times 10^{-3}$, 1.25×10^{-3}, 6.25×10^{-4}. The initial phase of generation of turbulent small scales, $t \lesssim 2$, has already been discussed in section V, Fig. 11, where two higher Reynolds number cases were also included. In the subsequent turbulent phase, $2 < t \lesssim 4$, dissipation rates are independent of η_0. At this time the kinetic energy has become small, $E^V/E^M < 0.2$. The small-scale turbulence in the X-point regions

decays and one is left with current sheets between coalescing flux tubes. At later times $T \gtrsim 5$, $\hat{\epsilon}$ significantly varies with η, scaling roughly as $\hat{\epsilon} \propto \eta^{\frac{1}{2}}$. The current sheets may become unstable, sporadically ejecting plasmoids, but this does not significantly enhance the dissipation rate.

VII Conclusions

We have presented results of high-resolution simulations of two-dimensional MHD turbulence. The most interesting features are, on the one hand, the η-independent energy dissipation rates and the inertial-range spectra consistent with the Kolmogorov $k^{-5/3}$ law (which is also measured in the solar wind, in contrast to Kraichnan's $k^{-3/2}$ prediction). On the other hand, there is a strong analogy to the behavior of two-dimensional hydrodynamic turbulence, regarding a) the transition from isolated vorticity gradient sheets with a k^{-4} energy spectrum to a turbulent state with $E_k \propto k^{-3}$, which corresponds to the transition from isolated current sheets with $E_k^{M,V} \propto k^{-2}$ to a small-scale turbulent state with $E_k^{M,V} \propto k^{-5/3}$ in the MHD case; b) the coexistence of turbulent and coherent structures, i.e. strong spatial intermittency, which is controlled by the magnitude of the vorticity in hydrodynamics and of the magnetic field in MHD. In addition, we find that the decay of a turbulent MHD flow proceeds in a statistically selfsimilar fashion if the initial kinetic energy is large enough $E^V(0)/E^M(0) \gtrsim 1$. This behavior is characterized by a constant ratio $E^V(t)/E^M(t) = c$, where c depends slightly on the velocity-magnetic field correlation and constant Reynolds numbers $R^V_{\Lambda,\lambda}(t)$, $R^M_{\Lambda,\lambda}(t)$. For lower initial kinetic energy $E^V(0)/E^M(0) < 0.5$, the turbulent phase is only transient, with E^V/E^M decreasing until the configuration becomes dominated by rather coherent coalescence processes.

Let us emphasize that the transition from single current sheet dissipation to dissipation via turbulent small-scale fluctuations, as illustrated in Figs. 10 and 11 in particular, is a smooth one, both processes coexisting in systems with different magnetic scales, depending on the local Reynolds number. While two flux tubes of small size may interact by a simple current sheet, the direct interaction between flux tubes of larger scale may lead to excitation of more uniformly distributed small-scale turbulence in their X-point regions. The coexistence of magnetic structures of largely different size is clearly seen in Fig. 18, that of different types of dissipative structures in Fig. 14a. Nor does the excitation of the tearing instability above a threshold Reynolds number lead to a sudden increase in the dissipation. This behavior corresponds to that of 3D turbulent systems, where with increasing Reynolds number increasingly smaller scales are excited so that the dissipation

rate is independent of the value of the dissipation coefficient. In fact, the difference between 2D and 3D MHD appears to be only a quantitative one, the main difference being that the "weak field" condition $\vec{k} \cdot \vec{B} \simeq 0$ can be satisfied virtually everywhere by small k_z components, for a strong B_z field component.

A final remark is made on the importance of these results to the theory of magnetic reconnection. While previous studies (see, for instance, Ref. 19), using relatively symmetric quasi-stationary conditions, reveal either steady-state current sheet reconnection or nonsteady but rather regular plasmoid formation (corresponding essentially to the coalescence phase discussed in section VI), the present investigations show that under more general conditions a turbulent, Reynolds-number-independent effective resistivity may be generated even in the framework of 2D incompressible MHD theory.

References

1) M.E. Brachet, M. Meneguzzi, and P.L. Sulem, Phys. Rev. Lett. 57, 683 (1986) ; M.E. Brachet, M.Meneguzzi, H. Politano, and P.L. Sulem, J. Fluid Mech. 194, 333 (1988)
2) J.C. McWilliams, J. Fluid Mech. 146, 21 (1984)
3) R. Benzi, S. Patarnello, and P. Santangelo, J. Phys. A: Math. Gen. 21, 1221 (1988)
4) B. Legras, P. Santangelo, and R. Benzi, Europhys. Lett. 5, 37 (1988)
5) A. Pouquet, J. Fluid Mech. 88, 1 (1978)
6) S.A. Orszag and C.M. Tang, J. Fluid Mech. 90, 129 (1979)
7) T.G. Cowling, Monthly Notices Roy. Astron. Soc. 94, 39 (1934)
8) A.N. Kolmogorov, C.R. Dokl. Acad. Sci. URSS 30, 301 (1941)
9) P.S. Iroshnikov, Astron. Zh. 40, 742 (1963) [Sov. Astron. 7, 568 (1964)]
10) R.H. Kraichnan, Phys. Fluids 8, 1385 (1965)
11) W.H. Matthaeus and D. Montgomery, Ann. N.Y. Acad. Sci. 357, 203 (1980)
12) A.C. Ting, W.H. Matthaeus, and D. Montgomery, Phys. Fluids 29, 3261 (1986)
13) M. Dobrowolny, A. Mangeney, and P.L. Veltri, Phys. Rev. Lett. 45, 144 (1980)
14) W.H. Matthaeus, M.L. Goldstein, and D. Montgomery, Phys. Rev. Lett. 51, 1484 (1983)
15) C. Canuto, M.Y. Hussaini, A. Quarteroni, and T.A. Zang, Spectral Methods in Fluid Dynamics, Springer Series in Computational Physics, New York 1988
16) D. Fyfe, G. Joyce, and D. Montgomery, J. Plasma Phys. 17, 317 (1977)
17) S. Kida and Y. Murakami, Phys. Fluids 30, 2030 (1987)
18) A. Pouquet, P.L. Sulem, and M. Meneguzzi, Phys. Fluids 31, 2635 (1988)
19) D. Biskamp, Phys. Fluids 29, 1520 (1986)
20) U. Frisch, A. Pouquet, P.L. Sulem, and M. Meneguzzi, J. Méc. Théor. Appl., 1983; special issue on two-dimensional turbulence, p. 191

Figure Captions

Fig. 1 Time evolution of a system with initial conditions A_2,
eq. (15), $\eta_0 = 6.25 \times 10^{-4}$, $M = 512$.
a) Total energy E and energy ratio E^V/E^M.
b), c) Reynolds numbers $R_\lambda^{M,V}$, $R_\Lambda^{M,V}$.

Fig. 2 η-scaling of magnetic Reynolds numbers for A_2 initial conditions :
$R_{\Lambda,\lambda}^M$ for $\eta_0 = 3.125 \times 10^{-4}$ —, 2 $R_{\Lambda,\lambda}^M$ for $\eta_0 = 6.25 \times 10^{-4}$ – – –, 4 $R_{\Lambda,\lambda}^M$ for $\eta_0 = 1.25 \times 10^{-3}$ – · – .

Fig. 3 Time evolution of a system with initial conditions B, eq. (16), with $H/E = 0.258$, $\eta_0 = 1.25 \times 10^{-3}$, $M = 512$. Diagnostics as in Fig. 1a,b,c.

Fig. 4 η-scaling of magnetic Reynolds numbers for B initial conditions :
$R_{\Lambda,\lambda}^M$ for $\eta_0 = 6.25 \times 10^{-4}$ —, 2 $R_{\Lambda,\lambda}^M$ for $\eta_0 = 1.25 \times 10^{-3}$ – – –, 4 $R_{\Lambda,\lambda}^M$ for $\eta_0 = 2.5 \times 10^{-3}$ – · – .

Fig. 5 E^V/E^M for two B-type realizations.

Fig. 6 Evolution of E, H, K for A_2 initial conditions :
a) $\eta_0 = 1.25 \times 10^{-3}$, b) $\eta_0 = 6.25 \times 10^{-4}$, c) $\eta_0 = 3.125 \times 10^{-4}$.

Fig. 7 Energy dissipation rate $\hat{\epsilon} = -d\,ln\,E/dt$ for the three A_2 cases as in Fig. 6.

Fig. 8 Energy dissipation rate $\hat{\epsilon}$ for the three B-type cases given in Fig. 4.

Fig. 9 ϵ/E^2 for the same cases as in Fig. 8.

Fig. 10 Generation of turbulent small-scale fluctuations.
j-contours for $\nu = 2$, $\eta_1 = 10^{-8}$, $M = 768$.
a) $t = 1.6$, b) $t = 2.1$.

Fig. 11 a) j-contours, b) ψ-contours at $t = 3$, same case as Fig. 10, illustrating the localization of small-scale turbulence in X-point regions of large-scale magnetic field.

Fig. 12 Tearing mode threshold. j-contours for two $\nu = 1$, $M = 768$ cases at $t = 2.1$, differing only in η_0, a) $\eta_0 = 3.125 \times 10^{-4}$, b) $\eta_0 = 6.25 \times 10^{-4}$.

Fig. 13 Energy dissipation rate ϵ for five cases, $\nu = 1$: $\eta_0 = 2.5 \times 10^{-3}$, 1.25×10^{-3}, 6.25×10^{-4}, 3.125×10^{-4} (upper 4 curves), $\nu = 2$, $\eta_1 = 10^{-8}$ (lower dashed curve), illustrating the two-stage saturation process.

Fig. 14 a) j-contours, b) ψ-contours for an A_2-type case with $\nu = 1$, $\eta_0 = 3.125 \times 10^{-4}$, $t = 8$.

Fig. 15 One-dimensional spectra $E^M_{\|k_x}$, $E^M_{\|k_y}$ for the state illustrated in Fig. 11.

Fig. 16 Radial energy spectra E^V_k, E^M_k for the state shown in Fig. 11.

Fig. 17 Normalized energy spectrum for a B-type $\nu = 1$ case taken at $t = 3,\ 4,\ 5,\ 6$.

Fig. 18 Normalized energy spectrum for a A_1-type $\nu = 2$ case taken at $t = 2.5, 2.6, 2.7, 2.8$. The straight line indicates the $k^{-5/3}$ dependence.

Fig. 19 ψ-contours for the B-type case, $\eta_0 = 6.25 \times 10^{-4}$, given in Figs. 4 and 8, at $t = 6$.

Fig. 20 $\hat{\epsilon}(t)$ for three A_1 cases, the upper three cases of Fig. 13.

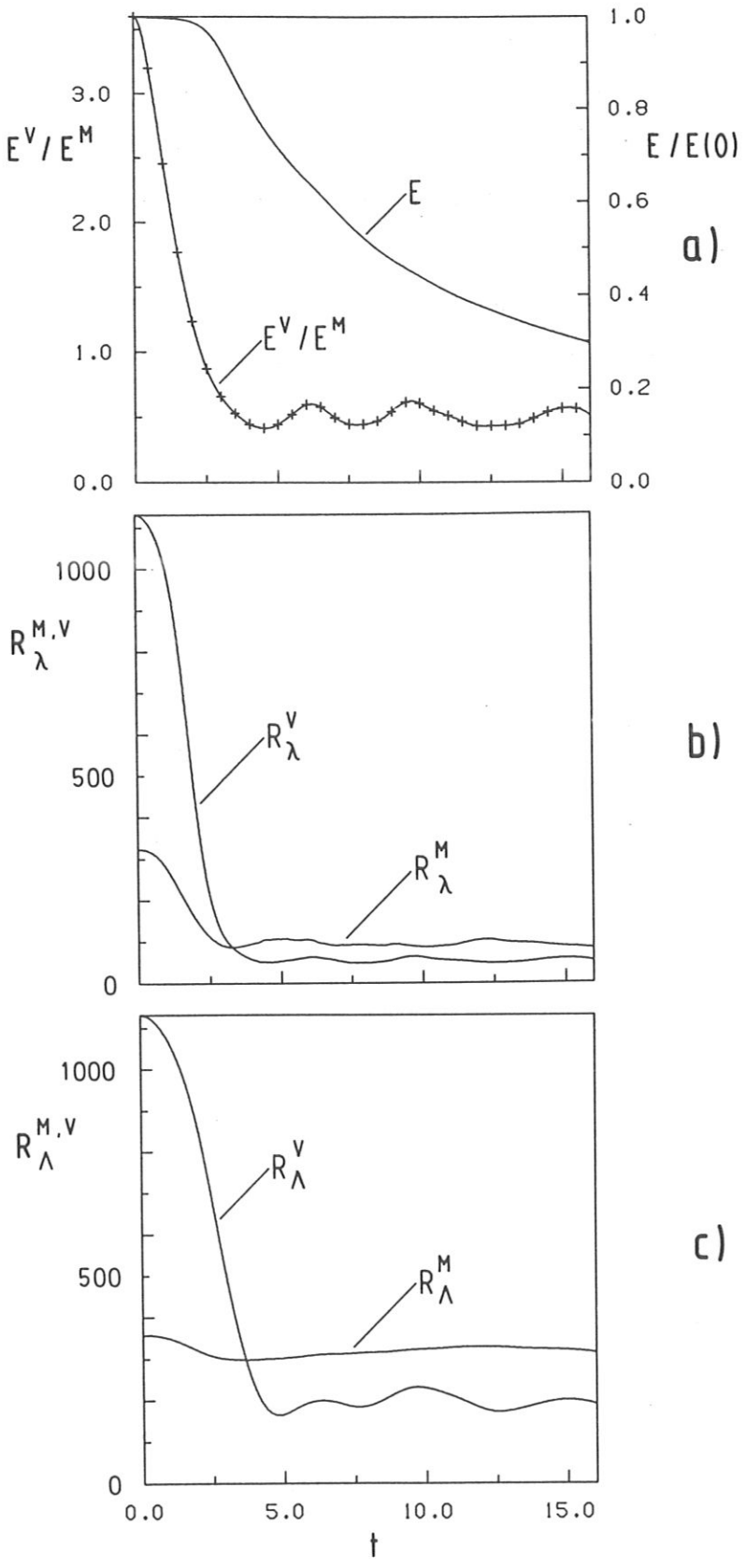
1.0
0.8
0.6
0.4
0.2
0.0
E / E(0)
3.0
2.0
1.0
0.0
E^V / E^M
E
E^V / E^M
a)
1000
500
0
R^M,V_λ
R^V_λ
R^M_λ
b)
1000
500
0
R^M,V_Λ
R^V_Λ
R^M_Λ
c)
0.0
5.0
10.0
15.0
t

Fig. 1

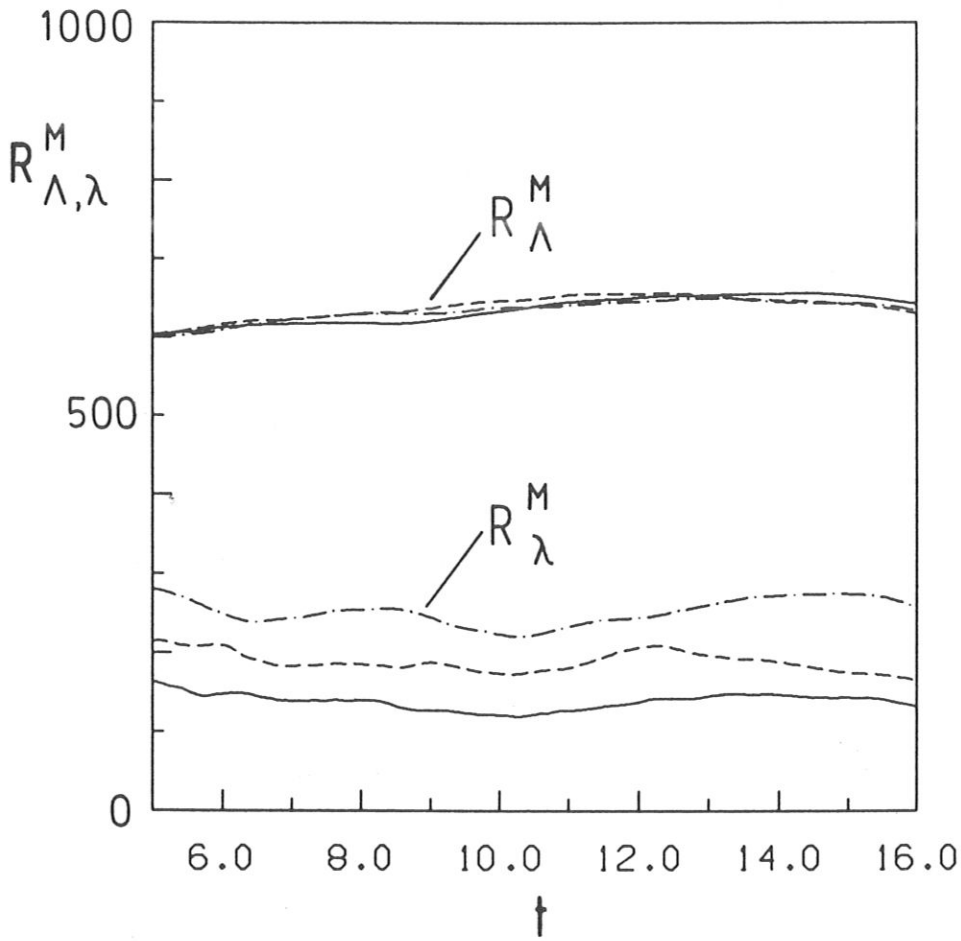
1000
500
0
$R^M_{\Lambda,\lambda}$
R^M_{Λ}
R^M_{λ}
6.0
8.0
10.0
12.0
14.0
16.0
t

Fig. 2

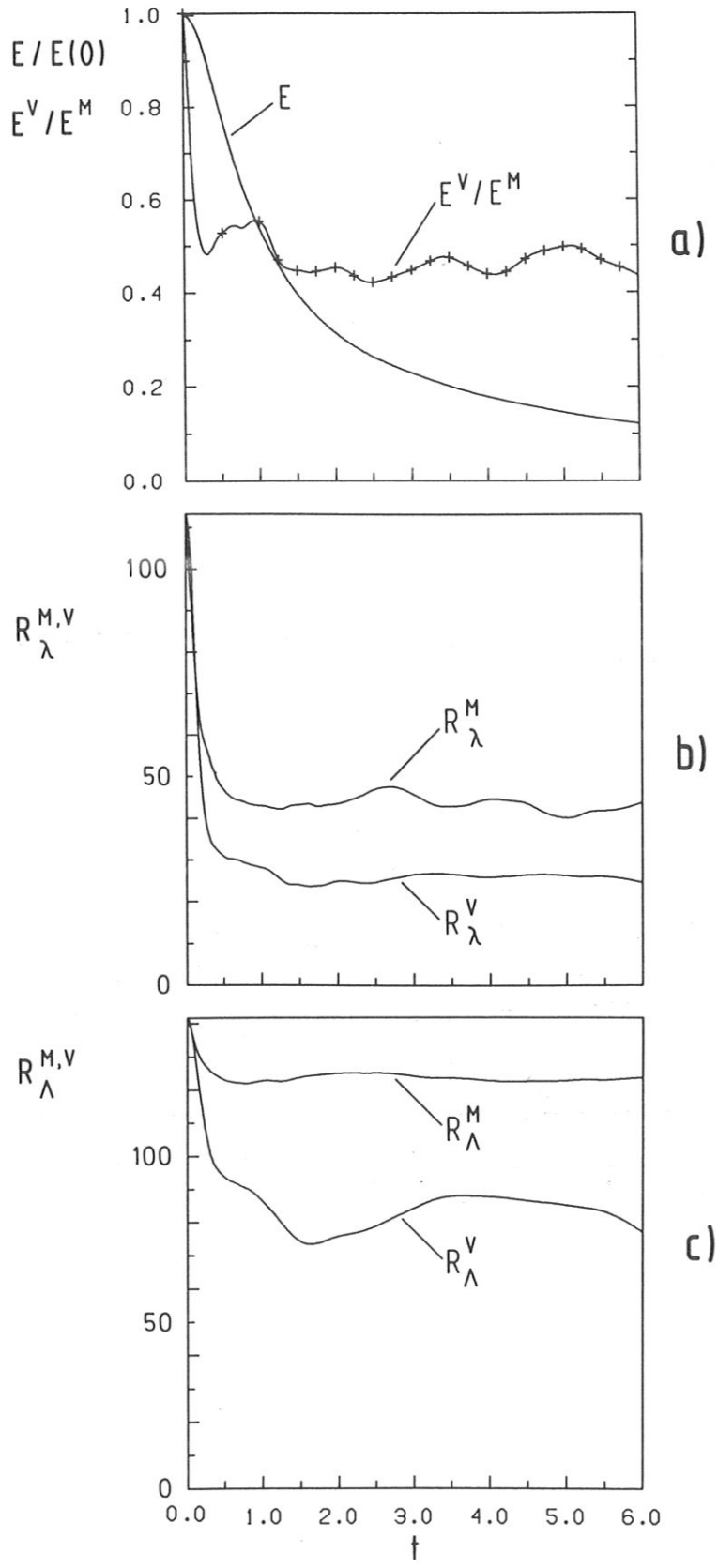
E / E(0)
E^V / E^M
1.0
0.8
0.6
0.4
0.2
0.0
E
E^V / E^M
a)
R^M,V λ
100
50
0
R^M λ
R^V λ
b)
R^M,V Λ
100
50
0
R^M Λ
R^V Λ
c)
0.0
1.0
2.0
3.0
4.0
5.0
6.0
t

Fig. 3

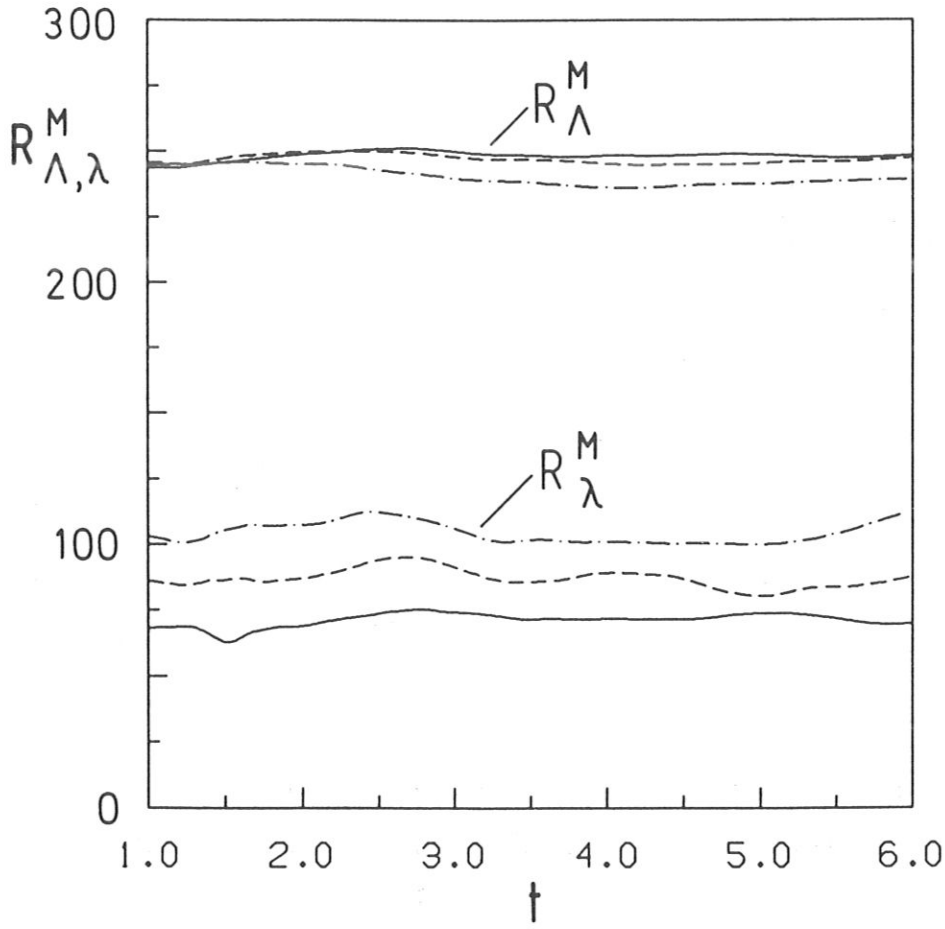
300
200
100
0
$R^M_{\Lambda,\lambda}$
R^M_Λ
R^M_λ
1.0
2.0
3.0
4.0
5.0
6.0
t

Fig. 4

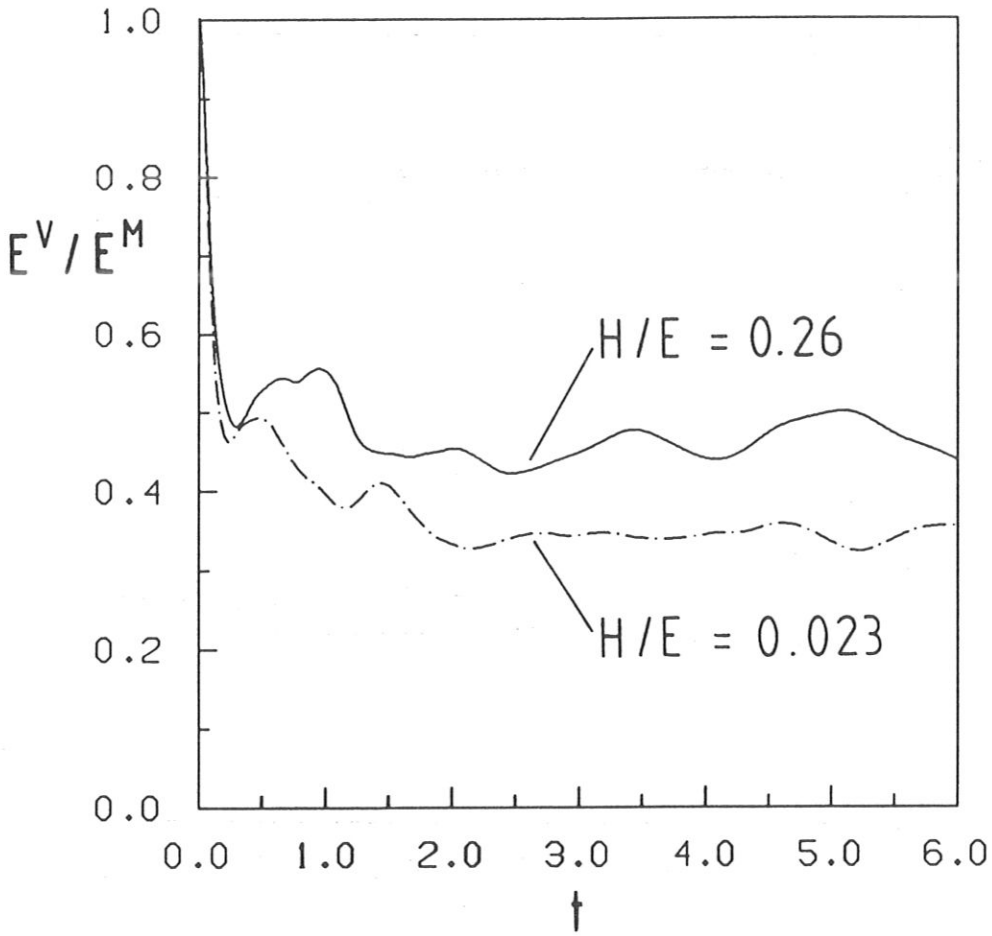

Fig. 5

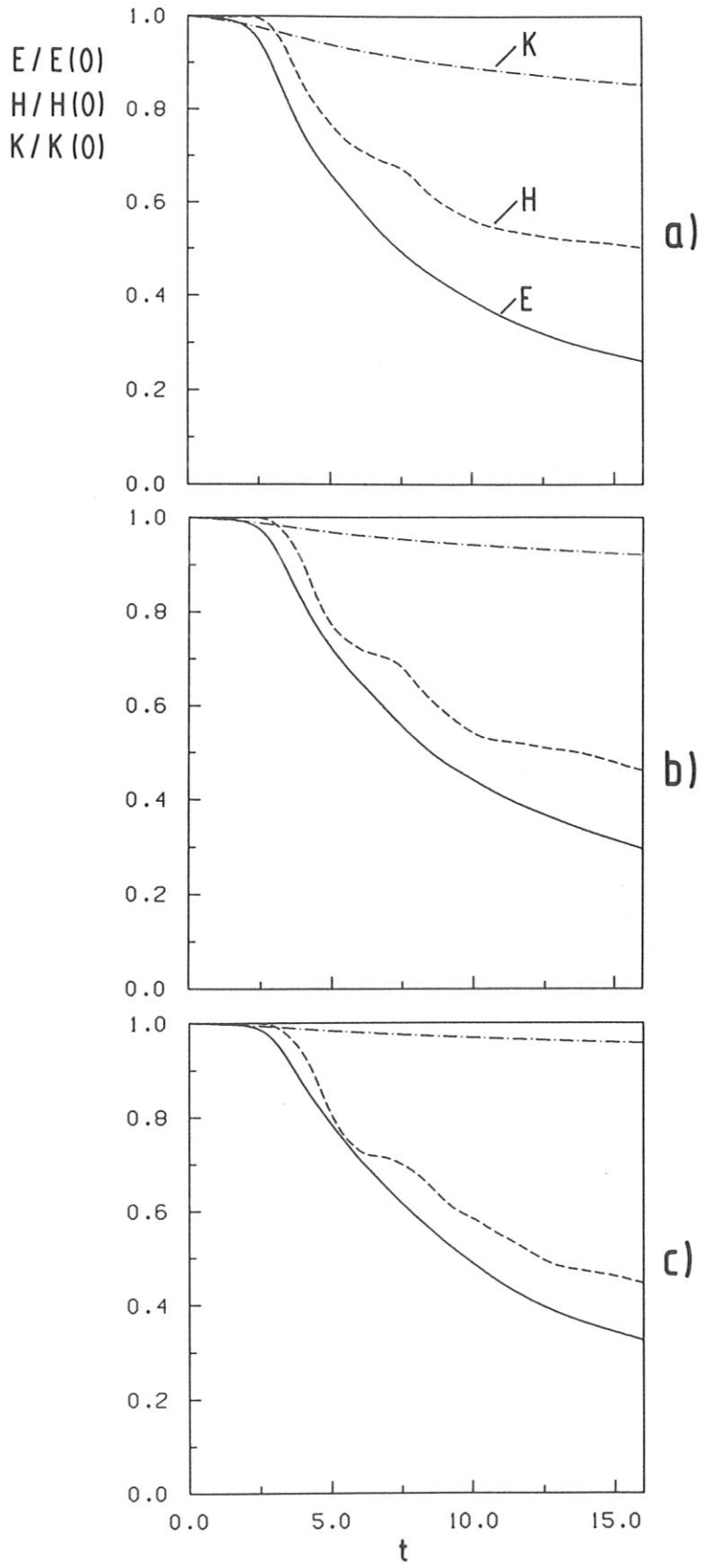

Fig. 6

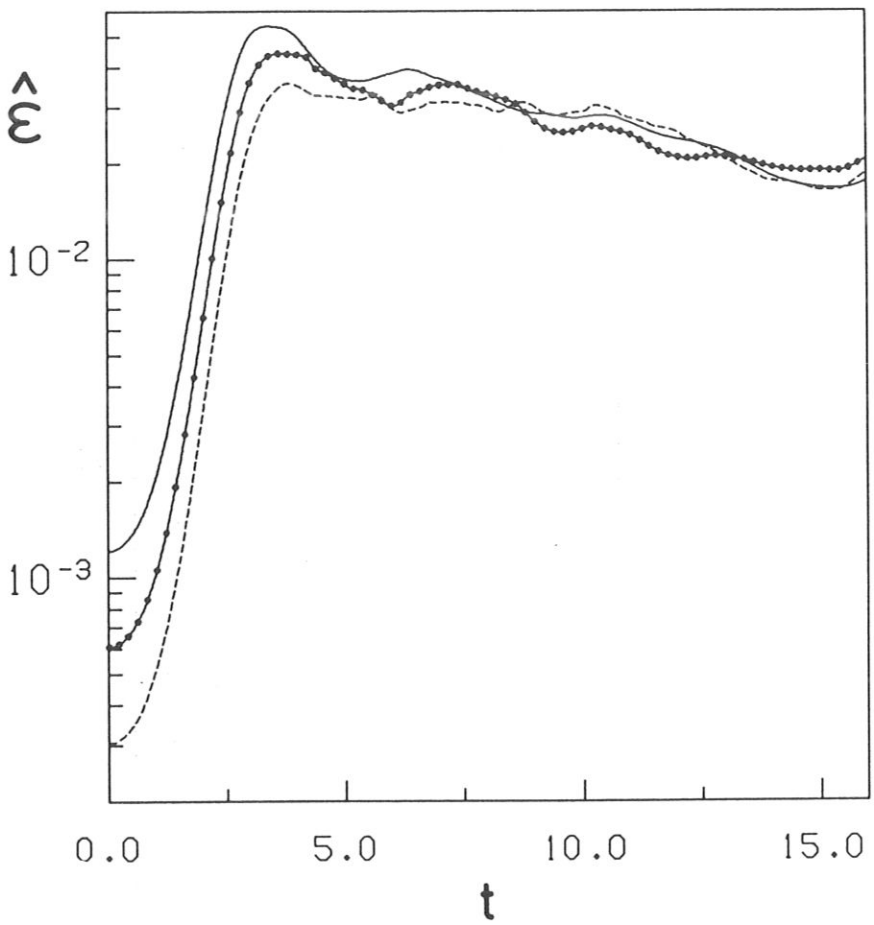

Fig. 7

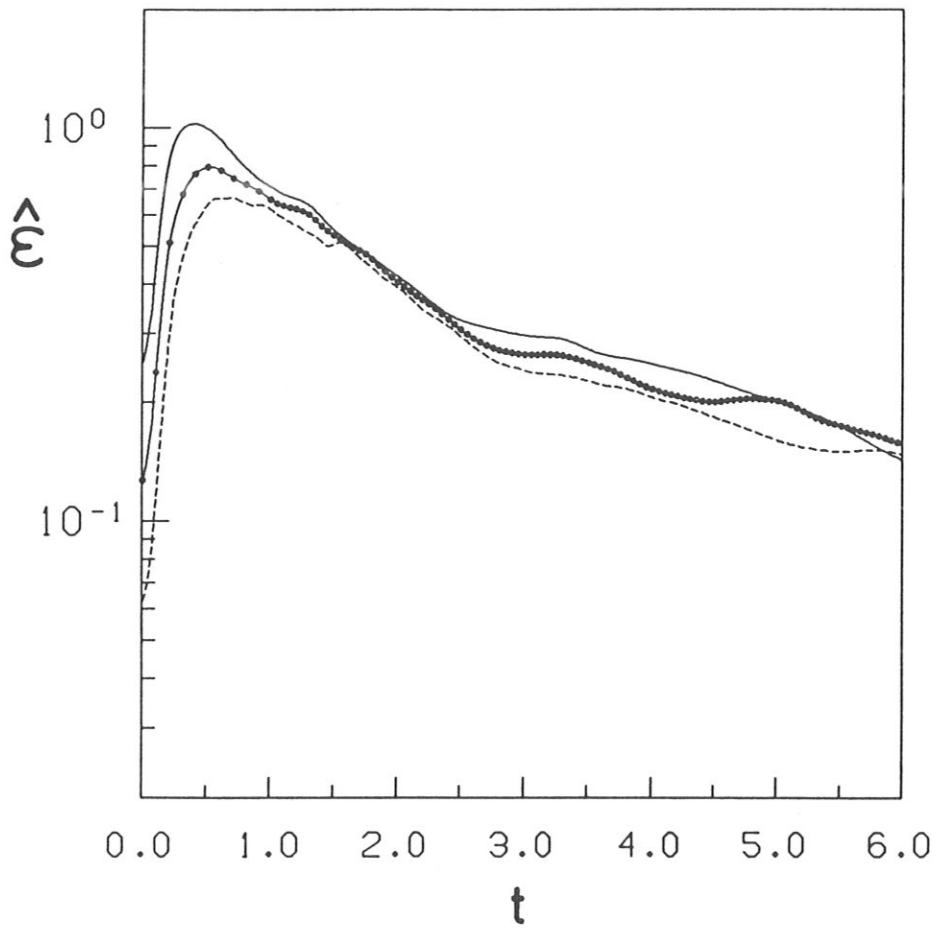

Fig. 8

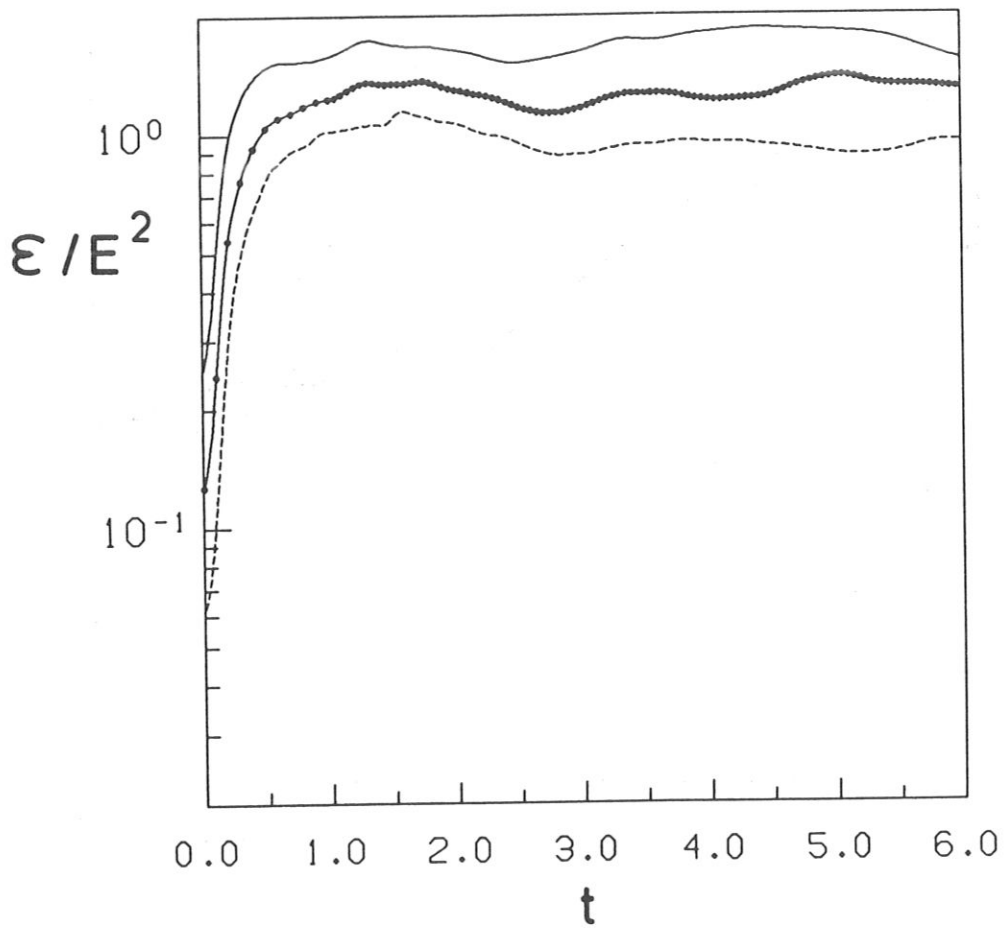

Fig. 9

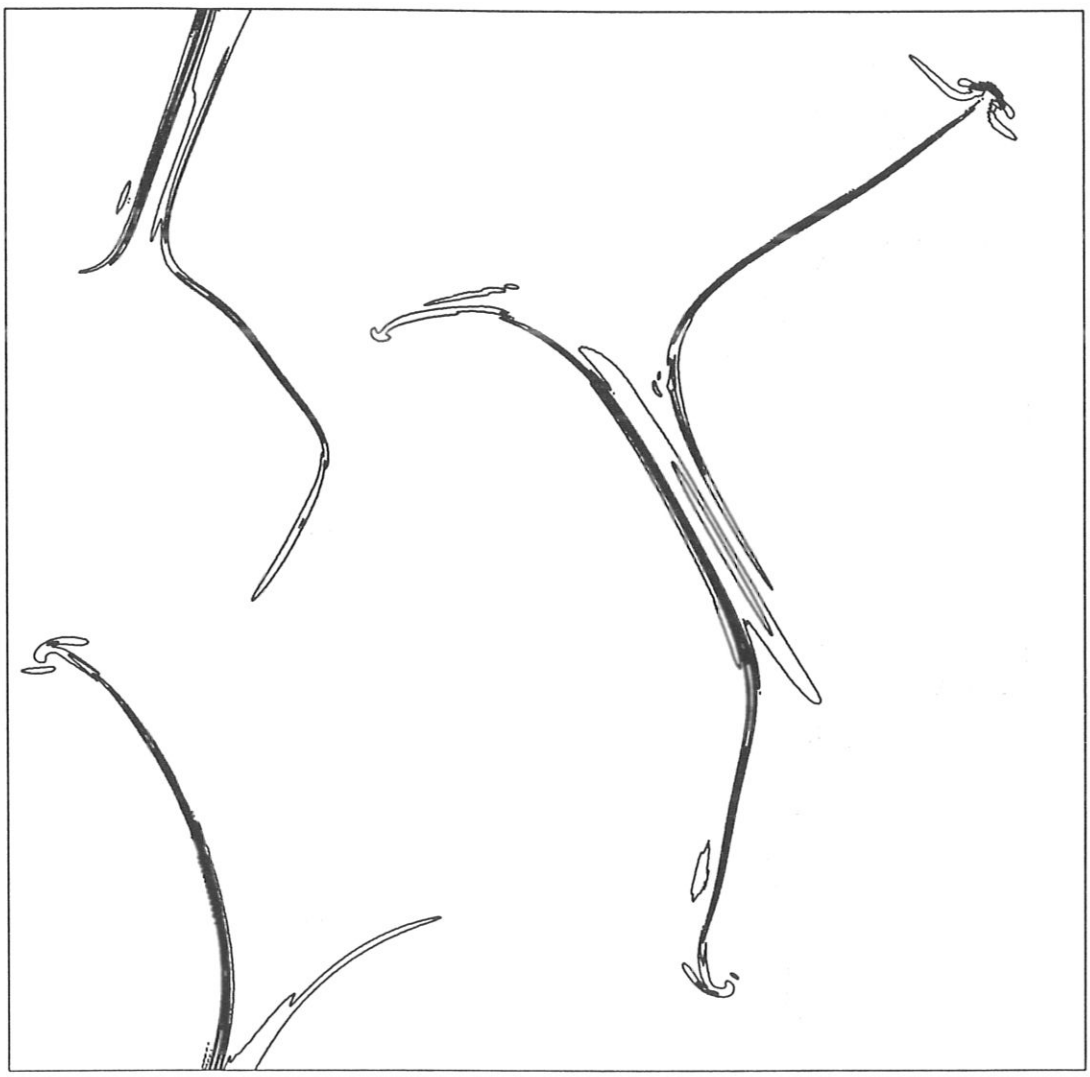

Fig. 10a

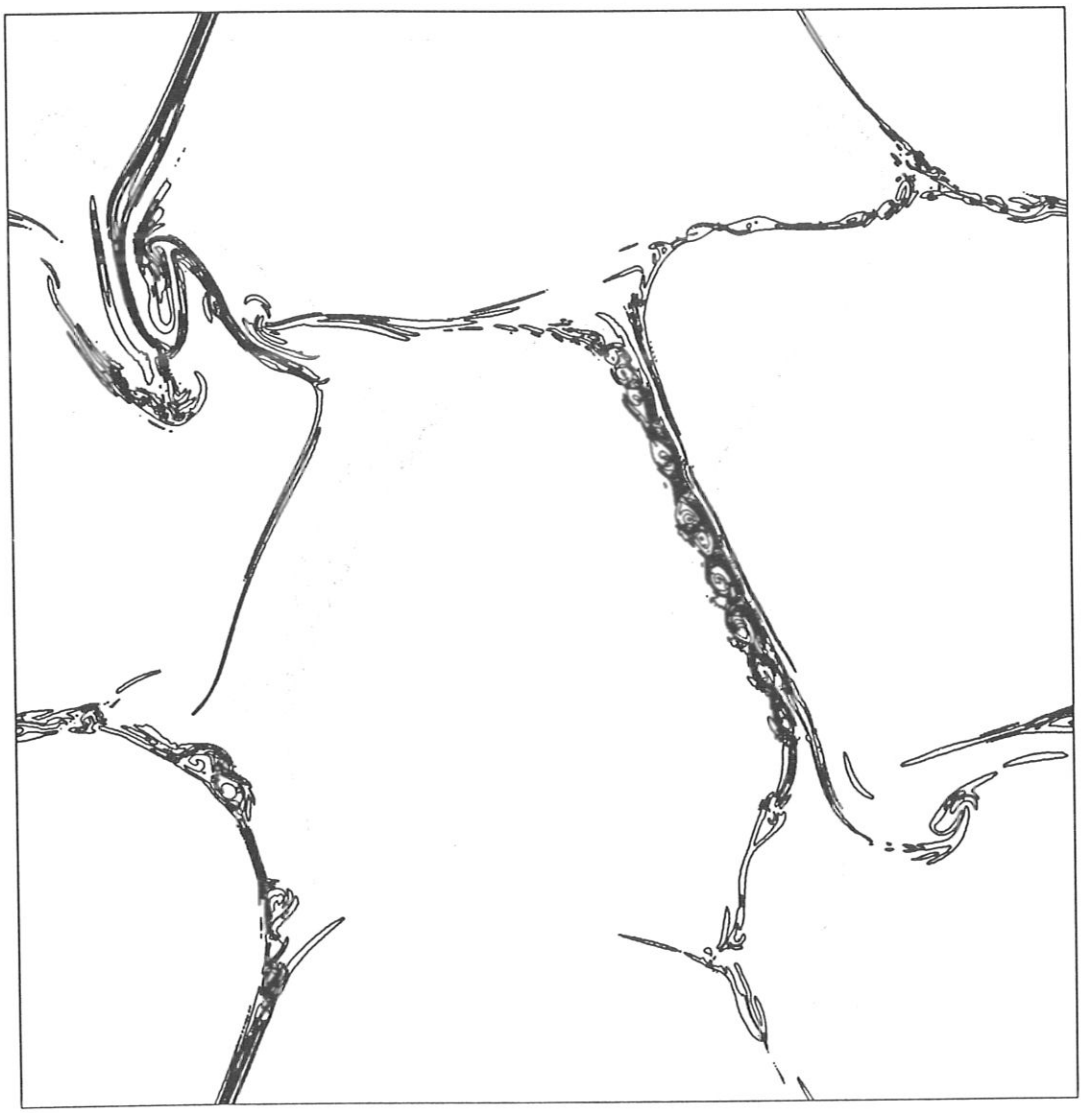

Fig. 10b

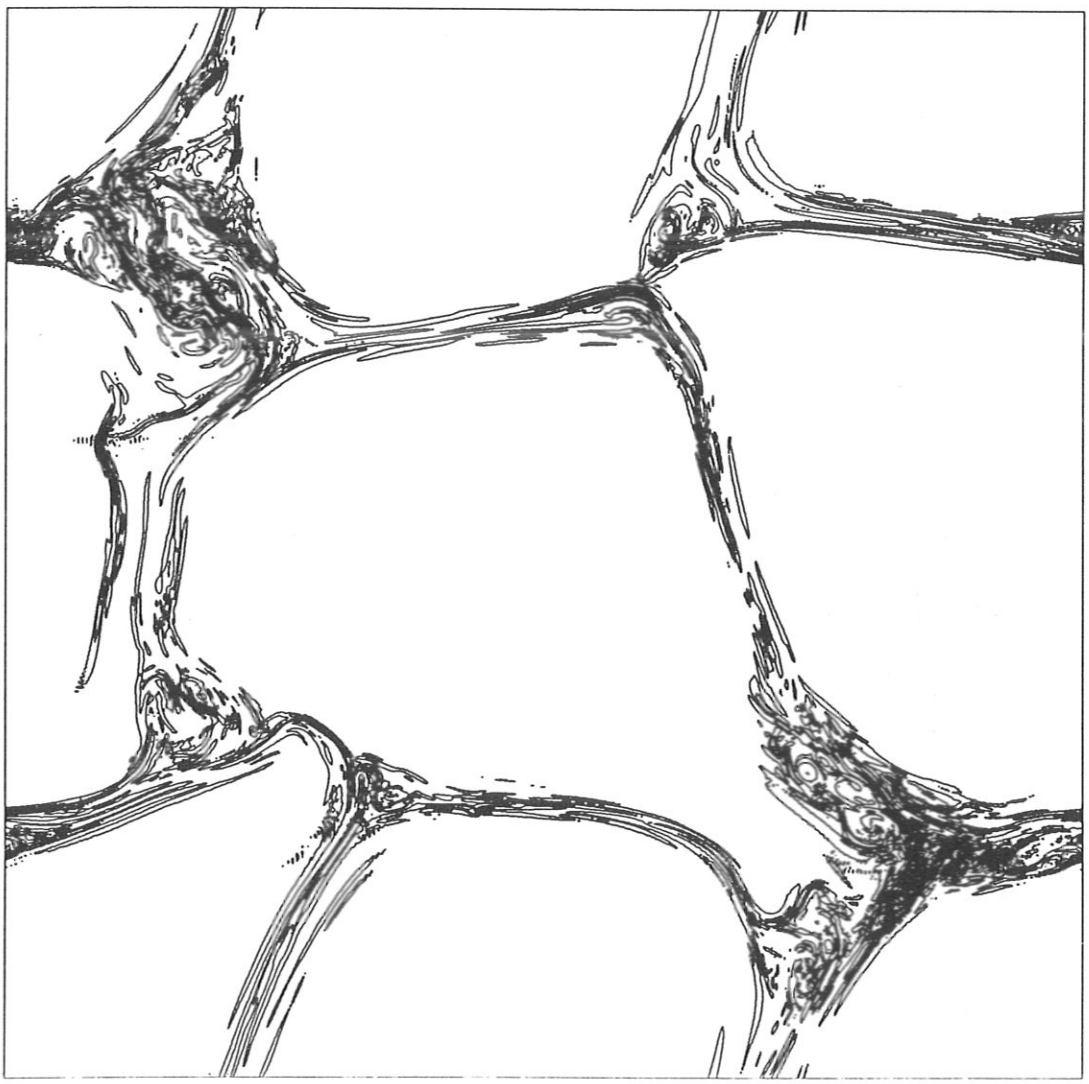

Fig. 11a

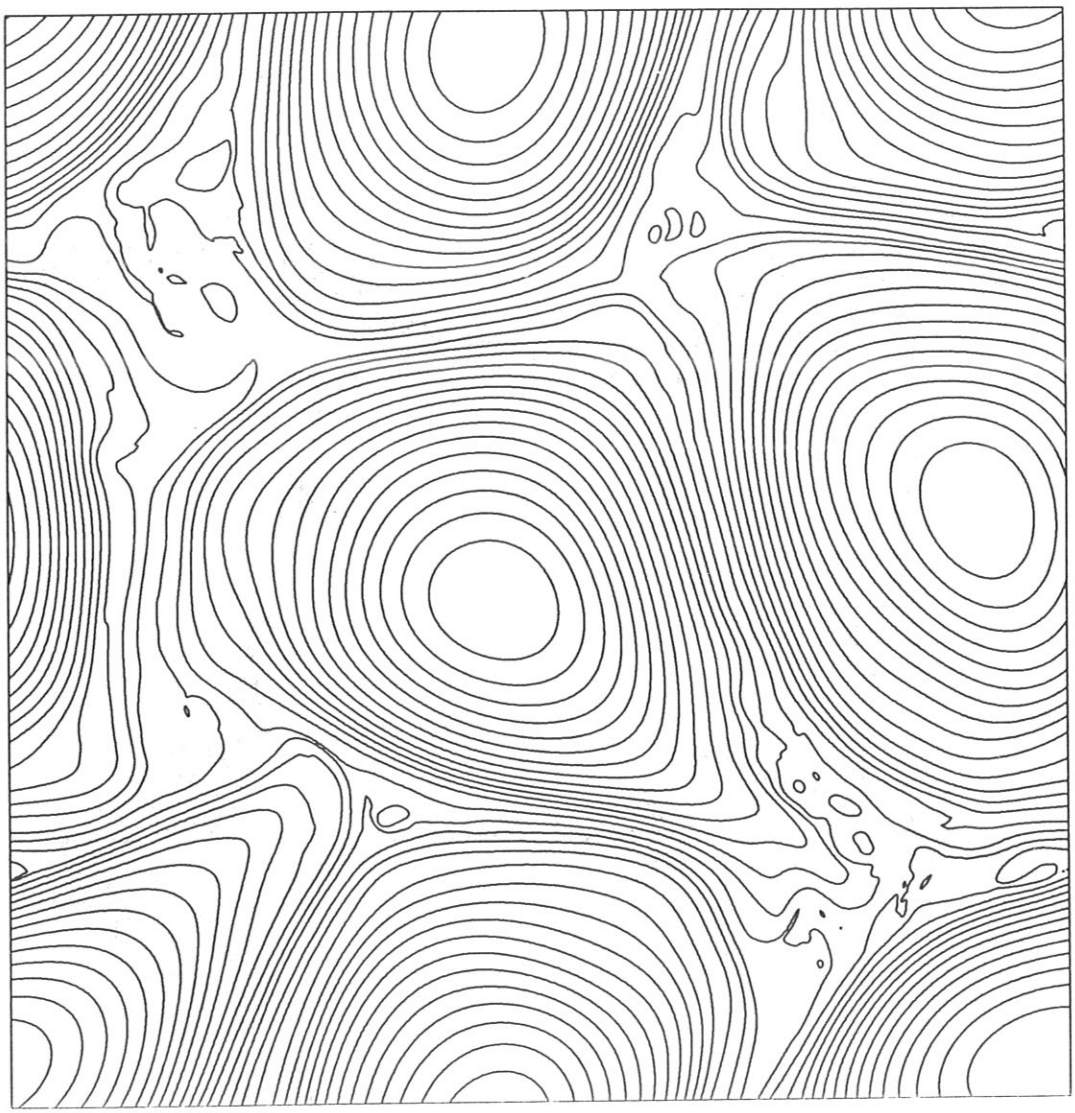

Fig. 11b

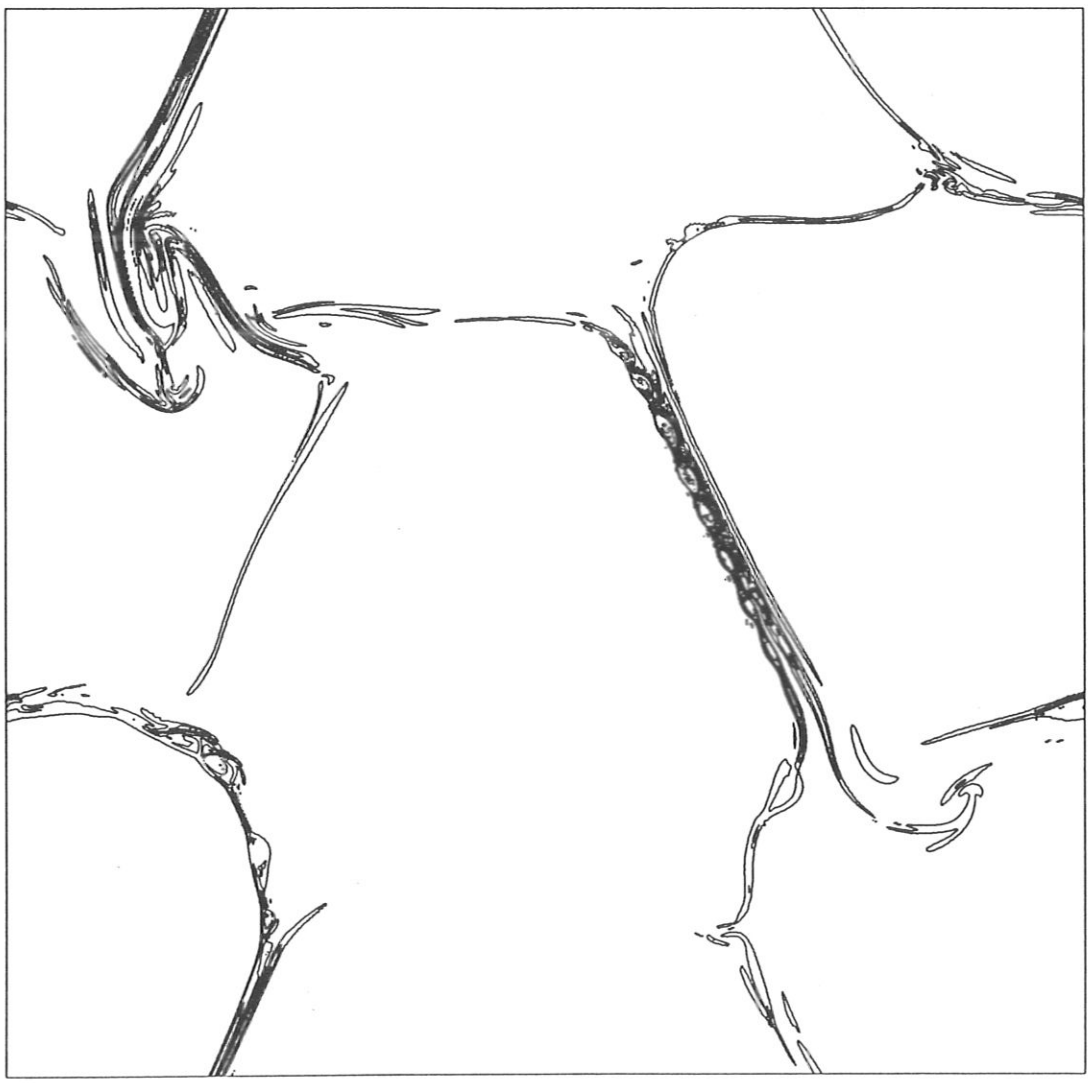

Fig. 12a

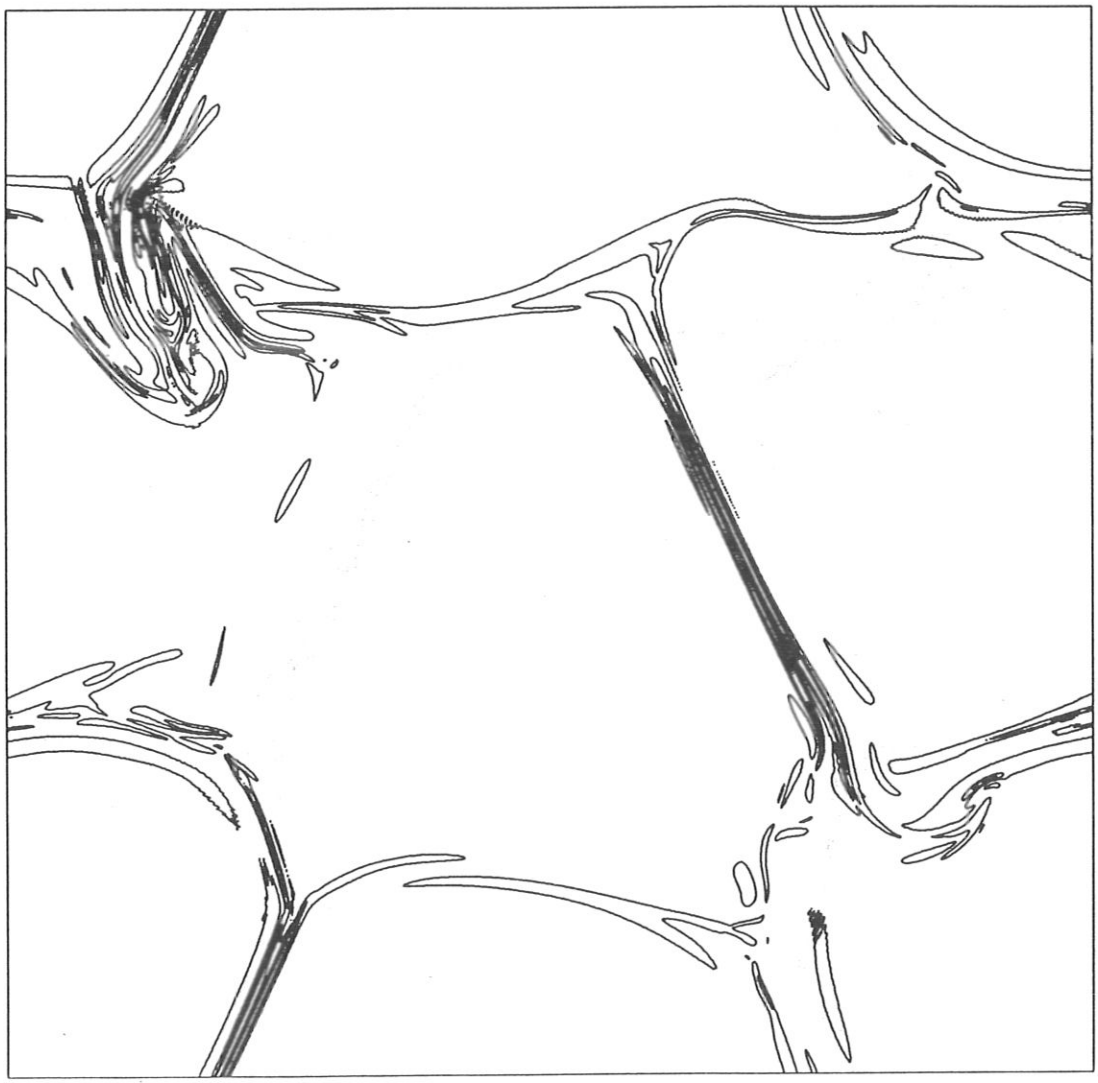

Fig. 12b

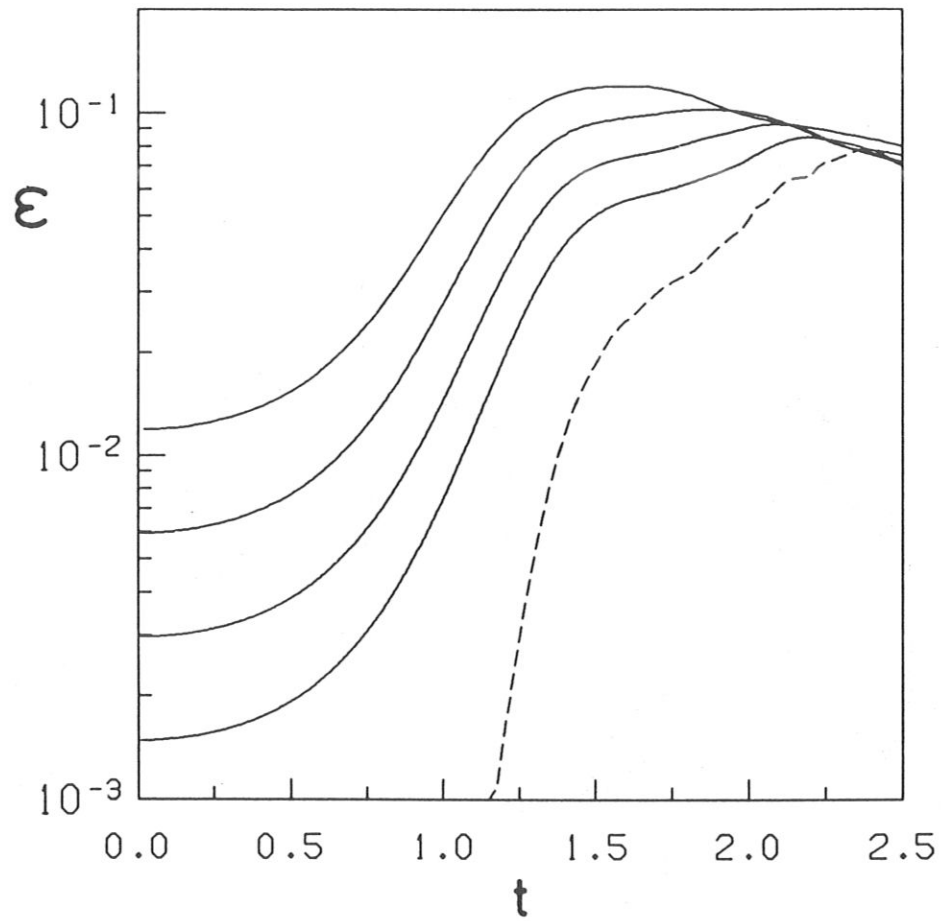

Fig. 13

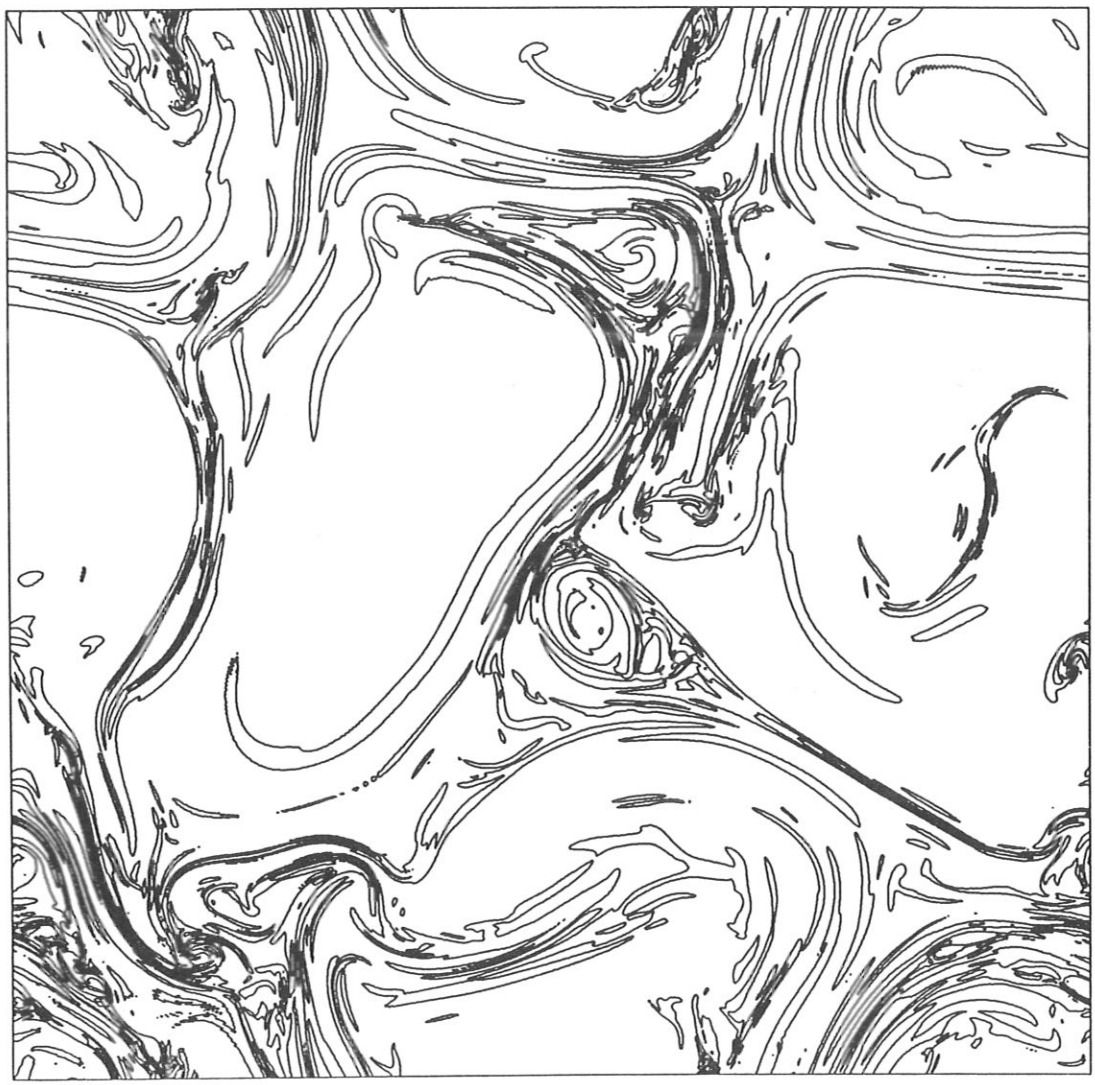

Fig. 14a

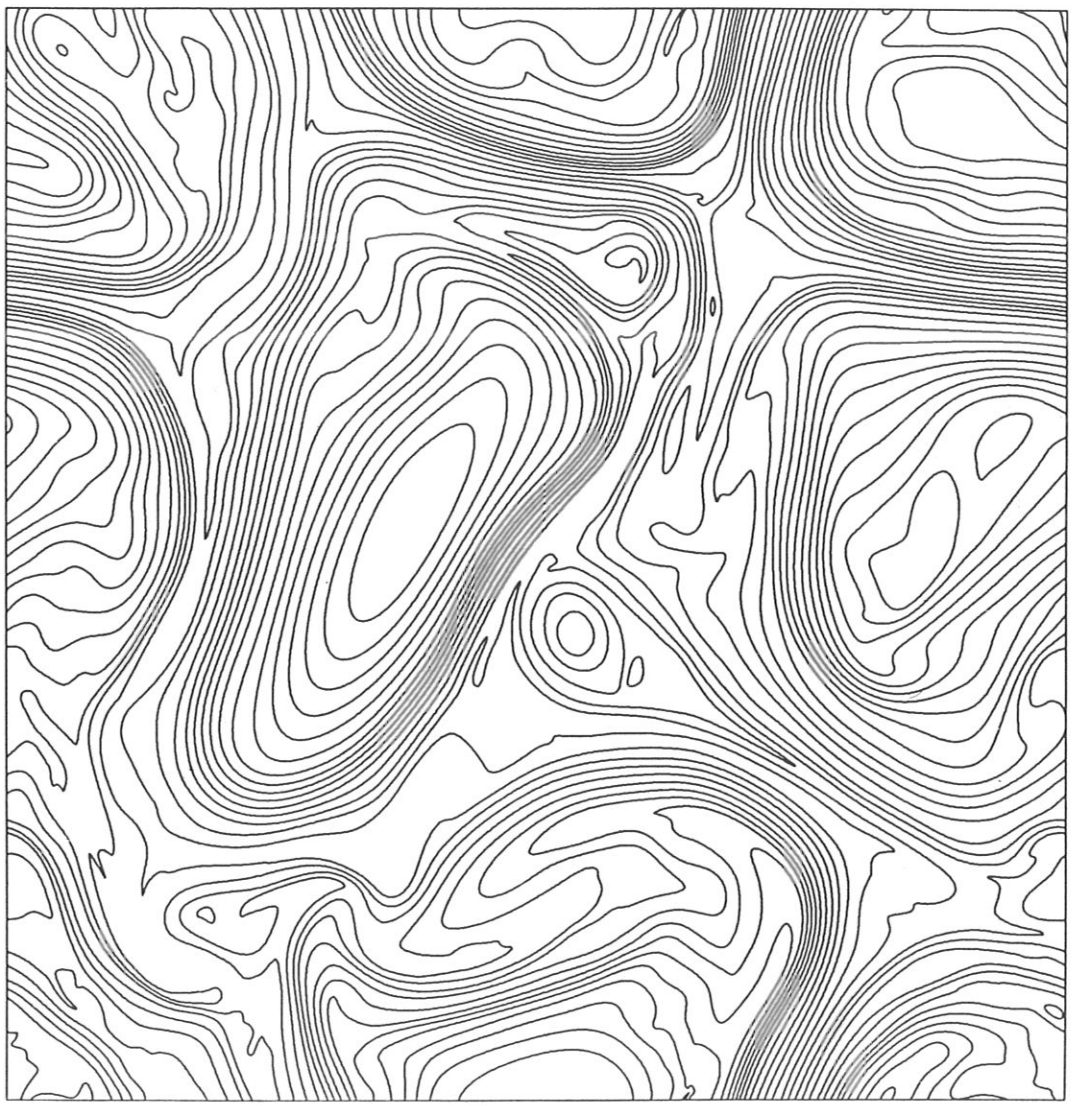

Fig. 14b

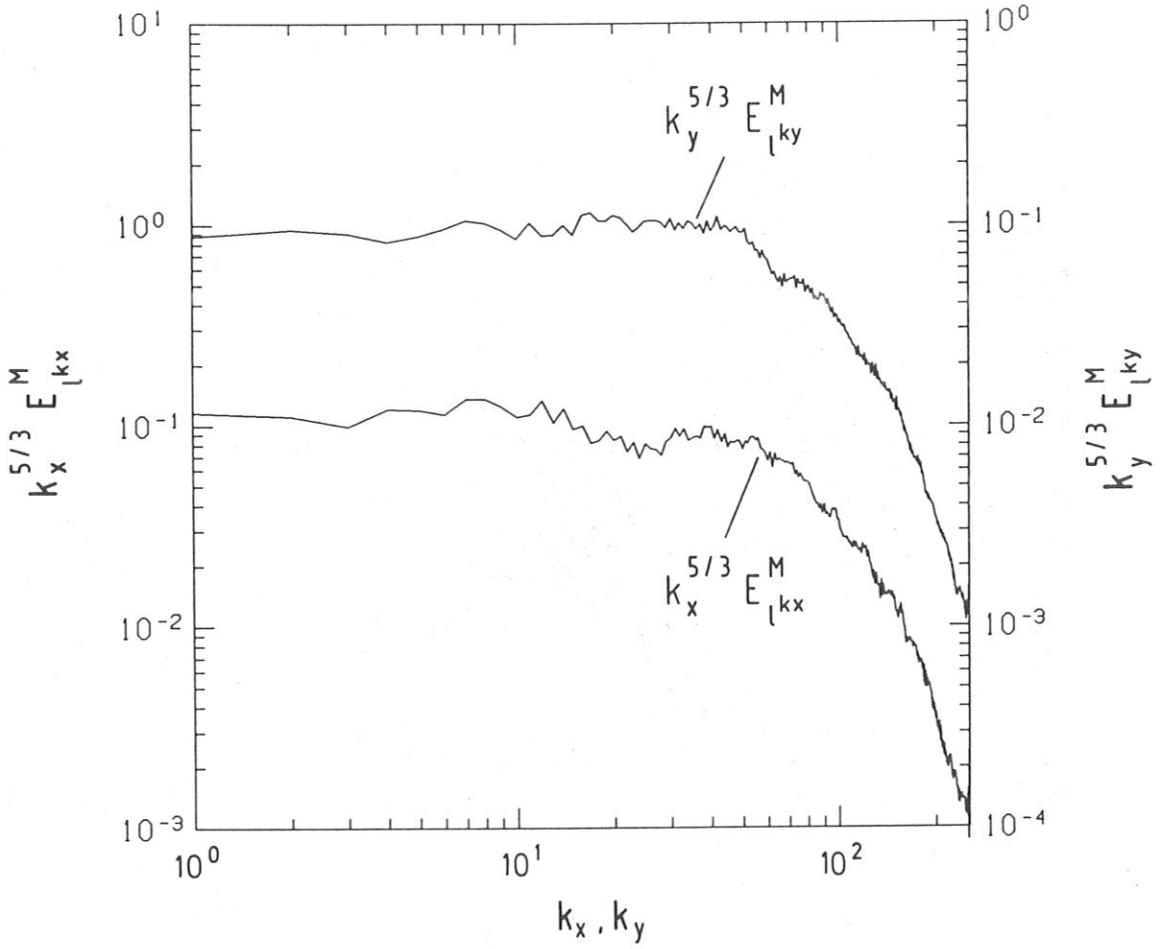
10^1
10^0
10^{-1}
10^{-2}
10^{-3}
10^0
10^1
10^2
k_x, k_y
$k_x^{5/3} E_{l^{kx}}^M$
$k_y^{5/3} E_{l^{ky}}^M$
$k_y^{5/3} E_{l^{ky}}^M$
$k_x^{5/3} E_{l^{kx}}^M$
10^0
10^{-1}
10^{-2}
10^{-3}
10^{-4}

Fig. 15

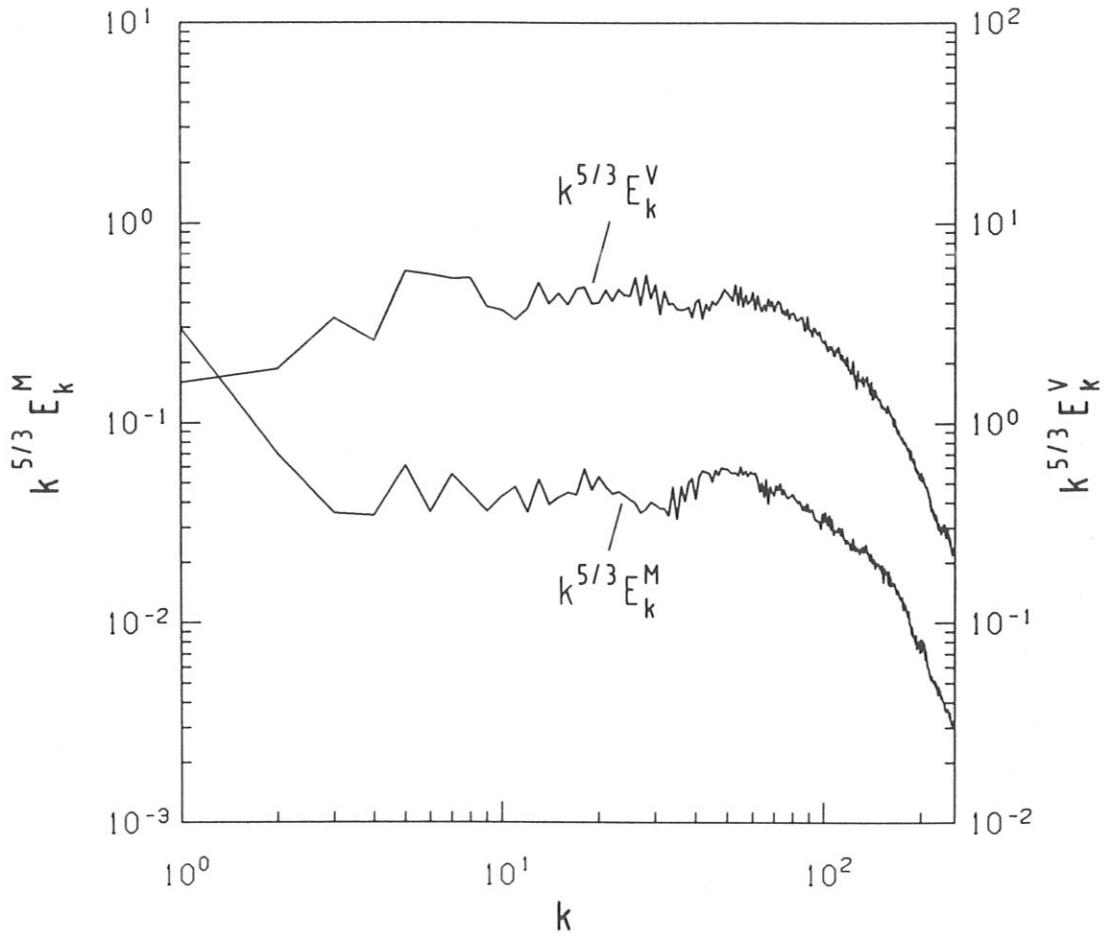
10^1
10^0
10^{-1}
10^{-2}
10^{-3}
10^2
10^1
10^0
10^{-1}
10^{-2}
10^0
10^1
10^2
k
$k^{5/3} E_k^V$
$k^{5/3} E_k^M$
$k^{5/3} E_k^M$
$k^{5/3} E_k^V$

Fig. 16

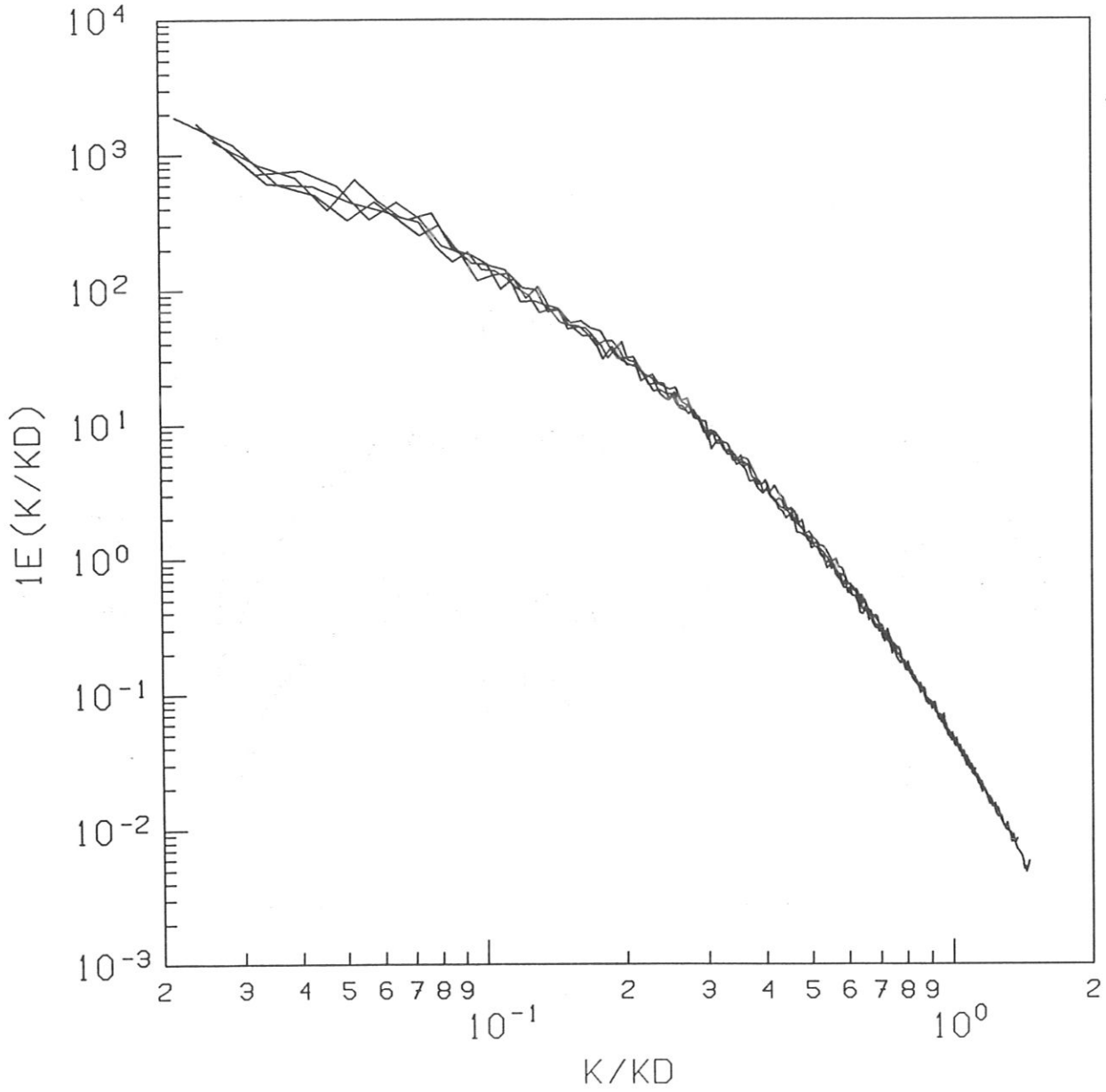
10^4
10^3
10^2
10^1
10^0
10^{-1}
10^{-2}
10^{-3}
1E(K/KD)
2 3 4 5 6 7 8 9
10^{-1}
2 3 4 5 6 7 8 9
10^0
2
K/KD

Fig. 17

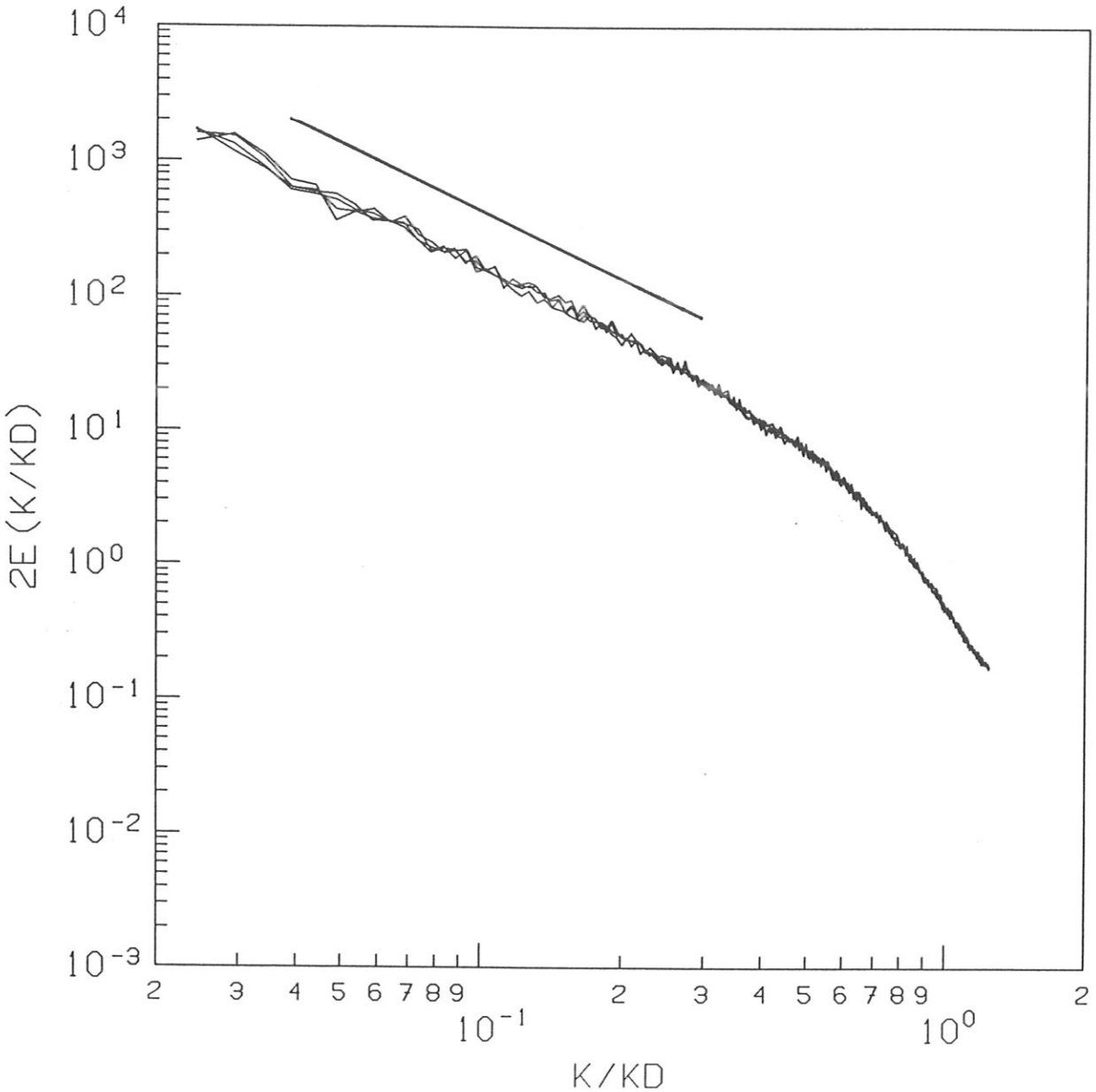
10^4
10^3
10^2
10^1
10^0
10^{-1}
10^{-2}
10^{-3}
2E(K/KD)
2 3 4 5 6 7 8 9
10^{-1}
2 3 4 5 6 7 8 9
10^0
2
K/KD

Fig. 18

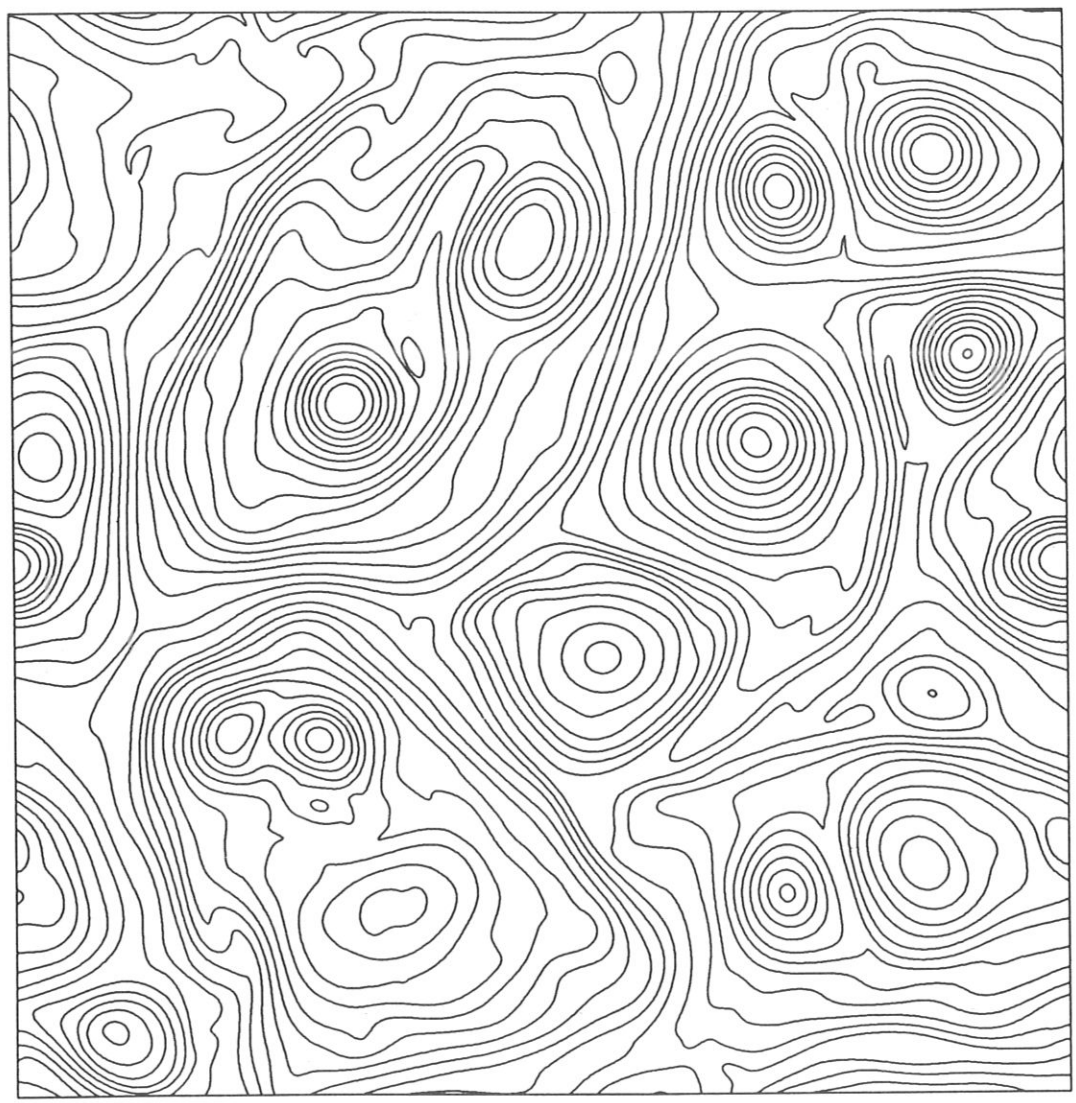

Fig. 19

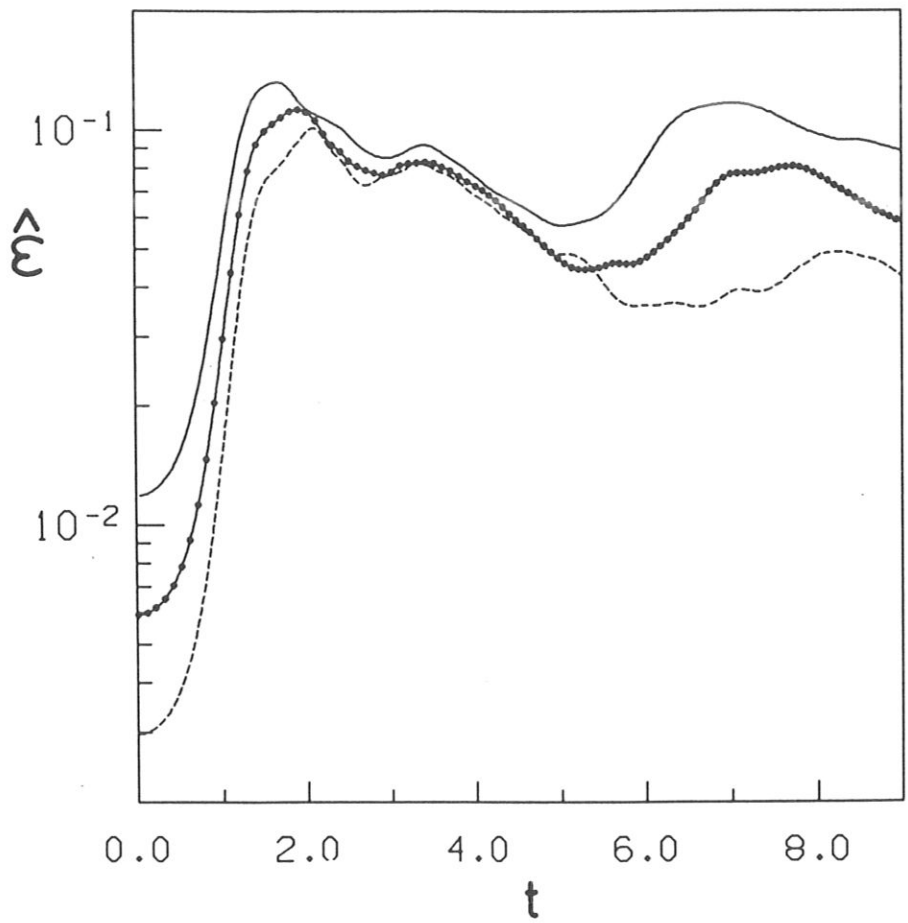

Fig. 20